Non-detection of Submillimeter Polarization by Rayleigh Scattering in Saturn's B-Ring

Andrew Srisuwananukorn

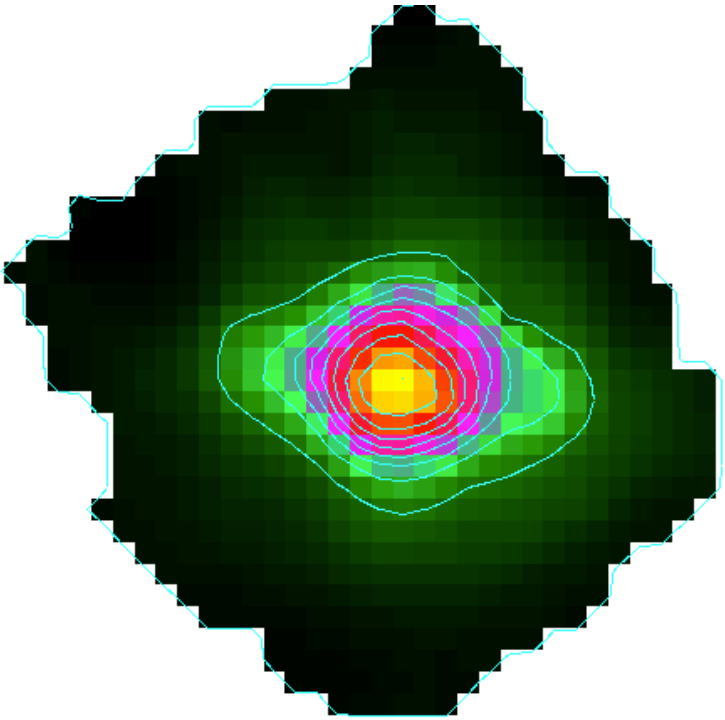

Senior Honors Thesis

Department of Physics and Astronomy

Weinberg College of Arts and Sciences

Northwestern University

Submitted 13 May 2013

Adviser: Dr. Giles Novak

Table of Contents

Chapter 1: Introduction:

Many of the greatest scientific theories have arisen as a direct result of novel observations. Alexander Fleming noticed the effects of penicillin on bacteria, resulting in man's first defense against these parasites. Arno Penzias and Robert Wilson first observed uniform radio signals from every direction in the sky, providing substantial evidence supporting theories regarding the origin of the universe. Henri Becquerel serendipitously found x-ray emissions of uranium samples with no apparent cause, the first observation to establish the concept of radioactivity. These discoveries changed society; however, the first step in these scientific leaps was the initial detection of new phenomena. My goal as an undergraduate research assistant is to provide the crucial initial information for phenomena never before detected, a goal I am able to pursue with the SHARP team under Dr. Giles Novak. In experimental astronomy, ground-based observations at submillimeter wavelengths are relatively novel, because the atmosphere only allows the transmission of a very narrow range of wavelengths.[1] Only at very dry observing sites can submillimeter measurements be detected.

In the following thesis, I will describe my work attempting to provide the first recorded observation of polarization by scattered light at submillimeter wavelengths for any astrophysical source. In particular, my project entailed observing the polarization of light scattered from the rings of Saturn at 350 and 450-micrometer (micron) wavelengths. The motivation for this specific source stems from Van der Tak et al, who detected a 30% polarization at 3.6 cm light, and 35% polarization at 6.1 cm light.[2] Novel detections of polarization at 350 and 450-micrometer wavelengths are scientifically useful; estimating the particle sizes from these measurements can support certain planetary formation theories. However, to understand my analysis of Saturn's rings, I must first explain two key phenomena: polarization and Rayleigh scattering.

---

[1] Hildebrand, R.H., Davidson, J.A., et al. 2000. A Primer on Far-Infrared Polarimetry. Publications of the Astronomical Society of the Pacific 112: 1215-1235. 1216.

[2] Van der Tak F., Pater, I., Silva, A., Millan, R. 1999. Time Variability in the Radio Brightness Distribution of Saturn. Icarus 142:125-147. 138.

1.1 Polarization:

Light waves are composed of an orthogonal combination of oscillating electiric and magnetic fields, as shown by Figure 1. [3] Linear polarization of an electromagnetic wave is the phenomenon where the electric field oscillates in only a single plane. As Figure 1 shows, the electric field of polarized light denoted in red is constrained to only the vertical plane. Thus, linearly polarized light is associated to a particular direction, as opposed to unpolarized light, which prefers no specific orientation. In discussing polarized electromagnetic waves, we choose by convention to discuss the orientation of the electric fields, not the magnetic fields. Though this choice is arbitrary, it is the convention used by all optics researchers. Light may also be circularly polarized,[4] but for sake of brevity, I will not discuss this phenomenon.

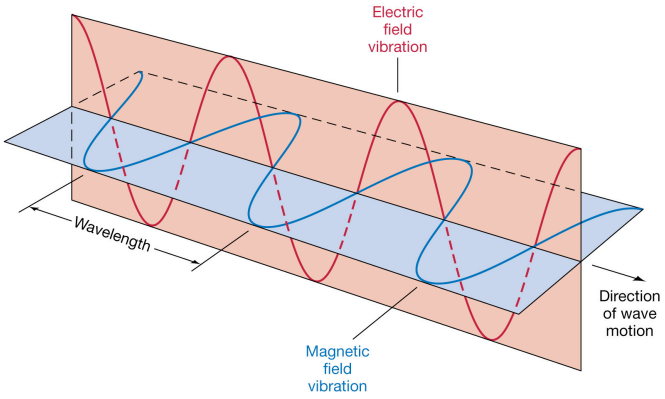

Figure 1: Polarized light. The electric field is given in red, while the magnetic field is given in blue.

1.2 Scattering:

It is understood that light scattered from small particles becomes polarized,[5] and that detection of polarization provides significant information about the particles themselves. As a familiar example, the blue sky arises from scattered blue light which is polarized. This phenomenon can be seen by viewing the sky through a polarizing filter (such as sunglasses). The inhomogeneities in the atmosphere scatter polarized blue light into our eyes, which polarizers held at varying angles may selectively allow or refuse transmittance. The sky can appear brighter or darker, depending on how the lenses are rotated. The light scattering that causes this polarization

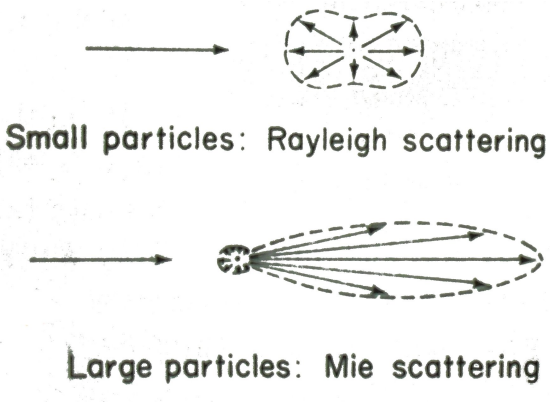

Figure 2: Rayleigh and Mie scattering.

[3] "Key Concepts of the Electromagnetic Wave." Journal of Informational Medicine. Web. 8 May 2013. <http://journalinformationalmedicine.org/keycon.htm>.
[4] Hildebrand et al. 2000. 1222.
[5] Van de Hulst, H.C. 1957. Light Scattering by Small Particles. New York, John Wiley & Sons Inc. 40.

can occur by either of two mechanisms. The distinction between the two situations is crucial for understanding this project.

As shown by Figure 2,[6] particles much larger than the wavelength of light scatter incident light preferentially in the forward direction. This phenomenon is defined to be Mie scattering. However, if the particle is comparable in size with the wavelength of incident light, the scattered light is emitted equally in all directions, which is Rayleigh scattering. To give a quantitative justification of this fact, Van de Hulst mentions that the intensity of Rayleigh scattering is given by the equation:[7]

$$I = \frac{\left((1+\cos^2\theta)\left(\frac{2\pi}{\lambda}\right)^4 |V\alpha'|^2\right)}{2r^2} I_0$$

In this equation, θ is the azimuthal angle in spherical coordinates, α is the dimensionless polarizability of the particle, V is the volume, and r is the distance away from observation.

The importance of this equation shows that the intensity of the scattered wavelength is inversely proportional to the fourth power of the wavelength, and proportional to the square of the volume.

$$I \propto V^2/\lambda^4$$

So for particles comparable in size to the wavelength, Rayleigh scattering is significant. As I will discuss in more detail later, polarization by Rayleigh scattering is the phenomenon I will look for in my analysis of Saturn's rings.

[6] Meyer-Arendt J.R. 1995. Introduction to Classical and Modern Optics. Englewood Cliffs, NJ: Prentice Hall. 279.

[7] Van de Hulst, 65.

1.3 Polarization by Rayleigh Scattering:

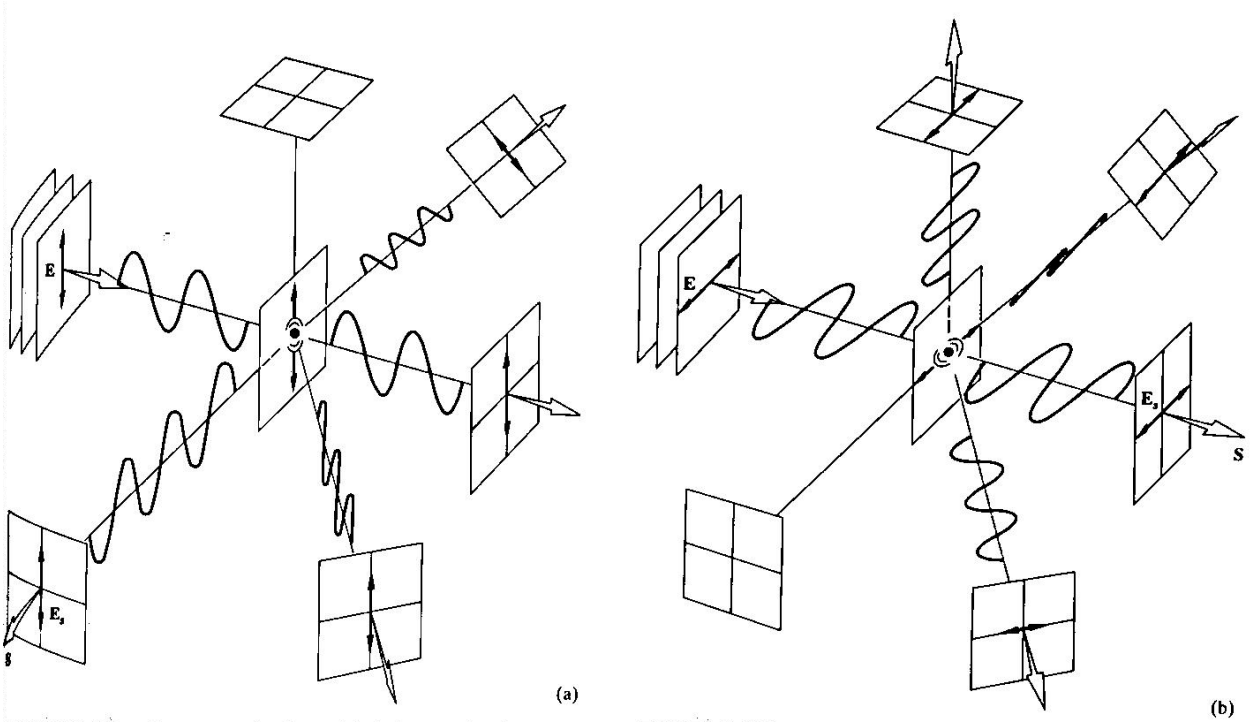

Figure 3: Rayleigh scattering due to two polarized incident electromagnetic waves.

The reason for polarization due to Rayleigh scattering is a purely geometric argument based on dipole radiation. Refer to the figure above from Hecht's Optics. In Figure 3,[8] the incoming radiation is polarized and is incident on some arbitrary particle in the center of the image. When the radiation interacts with the particle, the particle's electrons oscillate in the orientation of the incident electric field. This oscillating electron acts analogously to an electric dipole, which itself emits more electromagnetic radiation. Because of the specificity of oscillation direction, the emitted radiation is also polarized. However, notice from Figure 3 above that no radiation exists along the direction of oscillation (above the particle in the first image and in front of the particle in the second image).

[8] Hecht, E. 1998. *Optics*. Reading, MA: Addison Wesley Longman, Inc. 341.

The images of Figure 3 are the result of vertically and horizontally polarized light. However, consider the case of unpolarized light, which we can be thought of as a linear combination of vertically and horizontally polarized light. We can infer the result of Rayleigh scattered light from unpolarized incident light by overlapping both images of Figure 3.

In Figure 4, [9] the incident radiation is unpolarized, and when it interacts with the particle in the center, the electrons act similarly to two orthogonal dipoles. So as the figure shows, the light is polarized when looking from two directions: from above and from the front. This phenomenon is polarization by Rayleigh scattering.

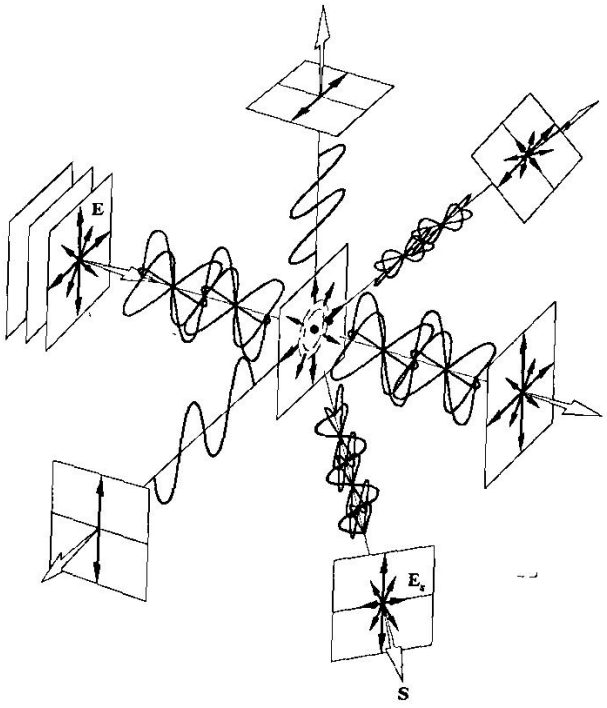

Figure 4: Rayleigh scattering of unpolarized light.

1.4 Submillimeter Wavelengths:

Analysis of submillimeter light is a relatively young scientific field, as not every wavelength of light can be observed from Earth. Because the atmosphere is partially or completely opaque to certain wavelengths, some wavelengths are absorbed by the atmosphere and cannot be detected from the ground.[10] To circumvent this issue, scientists attempt to get above the atmosphere with orbiting space telescopes, balloon-borne experiments, or establishing telescopes at unusually high and dry observing sites. As part of the SHARP team at Northwestern University, we utilize the latter option with the Caltech Submillimeter Observatory at the 14,000-foot summit of Mauna Kea on the island of Hawaii.

[9] Hecht, 342.
[10] Hildebrand et al., 1216.

As Figure 5 shows,[11] the atmosphere allows certain wavelengths to transmit through more efficiently than others. At 350 and 450 μm, the transmittance of the atmosphere is relatively high for very dry observing sites. Because the range of available wavelengths is so narrow and because one requires unusual observing conditions, astronomy at submillimeter wavelengths is a relatively new field.

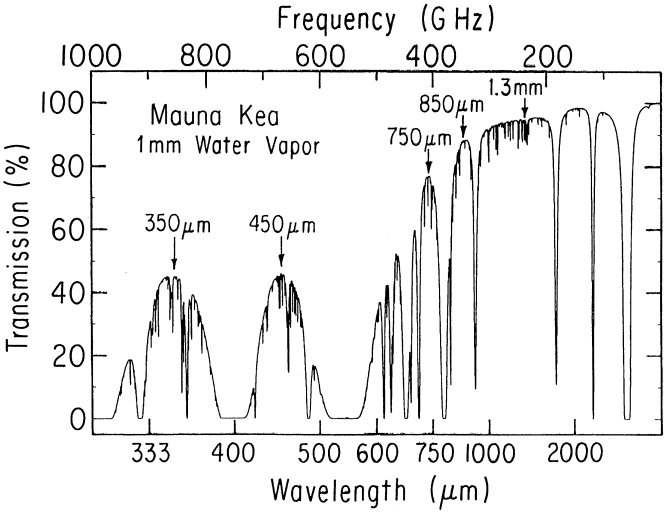

Figure 5: Atmospheric transmittance at 4.2 km made by Hildebrand et al.

1.5 Saturn's Rings:

Besides its scientific novelty, the polarization of scattered submillimeter light can provide crucial information regarding the sizes of the particles that comprise a source. In particular, knowledge concerning this size distribution will allow for a better understanding of the origin of planets. A possible first step in planet formation occurs when interstellar dust grains, the miniscule bits of solid matter that inhabit the interstellar medium (ISM), coagulate into larger solid particles.[12] Adhesion forces between the interstellar dust (having sizes below 1 μm or 10^{-6} meters) are thought to cause them to aggregate to a size above 1 mm (10^{-3} meters). Therefore, observing particles of submillimeter size (between 1 μm and 1 mm) should help us to test planet formation theories.

Scientists have attempted to analyze the particles of this intermediate size within protoplanetary disks—a stage in star formation when planets are believed to be forming. As Krejny points out, the observed 350 μ m polarization of a T Tauri disk (a nearby protoplanetary disk) is below 1.7%, thus undetectable with current technology. However, I have analyzed a system much closer than Krejny's target and hope to attain a more

11 Hildebrand et al., 1216.

12 Krejny, M., Matthews T., Novak, G., Cho, J., Li, H., Shinnaga, H., Vaillancourt, J.E. 2009. Polarimetry of DG Tau at 350 m. The Astrophysical Journal 705: 717-722. 717.

accurate upper limit. Because of its similarity to protoplanetary disks, I have studied the particle size distribution within Saturn's rings via submillimeter polarimetry.

The motivation to analyze Saturn's rings stems from the similarity of Saturn to protoplanetary disks. Because Saturn is relatively close to Earth compared to other disk-like systems, Saturn gives a very bright, strong signal for much easier analysis. However, the origin of Saturn's rings is still widely debated; we still do not know when these rings formed, which is crucial to planetary evolution theory.[13] Two of the key parameters for classification of Saturn's rings are position and composition.

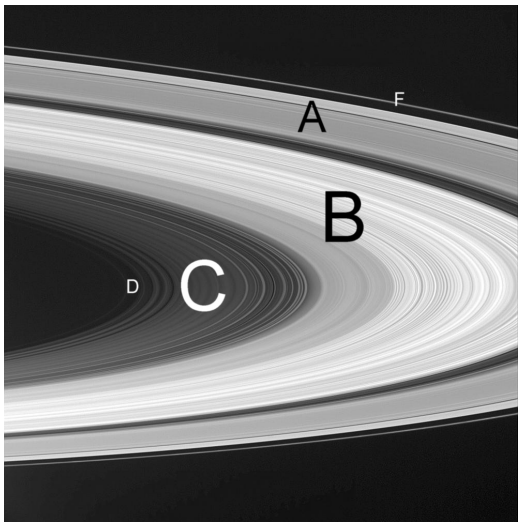

Figure 6: Classification of Saturn's rings. The outermost ring is classified as the F-ring.

Esposito notes that larger particles tend to be "agglomerates of smaller elements that are at least temporarily cohering." On the other hand, smaller particles imply a collisional process, where collisions between larger bodies create dust and pebbles. Knowing the particle size distribution within the rings will tell us which mechanism is dominant; collisional processes or gravitational aggregation.

Using modeling techniques, Vahidinia et al. mention that most particles in the outer rings like the F-ring lie in the range of 10-30 μm (10^{-6} meters).[14] Schmidt et al. also mention that the minimum size of particles in every other ring is at least 1 cm (10^{-3} meters).[15] With the technology and resources available to me, I hope to observe the particles in the intermediate range, particles in the size range of 100 μm – 1 mm, and shed new light on the intermediate processes that separate smaller and larger particles. This is a pressing issue to which scientists have devoted many resources. The Cassini-Huygens spacecraft was launched specifically to study Saturn's rings and orbiting satellites. The Visible and

[13] Esposito, L.W. 2010. Composition, Structure, Dynamics, and Evolution of Saturn's Rings. *Annual Review of Earth and Planetary Sciences* 38: 383-410. 385.
[14] Vahidinia S., et al. 2011. Saturn's F Ring Grains: Aggregates are Made of Crystalline Water Ice. *Icarus* 215:682-694. 693.
[15] Schmidt J, et al. 2009. Dynamics of Saturn's dense rings. See Dougherty et al. 2009, pp. 413–58.

Infrared Mapping Spectrometer (VIMS) was installed into Cassini to study the composition and structure within the rings. The topic of particle size is still under debate.

Most data on Saturn's rings stem from VIMS, a spectrometer that observes the absorption and emission lines of matter in Saturn's rings. However, Hedman et al. conclude that size distribution cannot be obtained by using transmission methods alone.[16] Besides the novelty of submillimeter analysis, another method quickly gaining interest within astronomy is polarimetry, my proposed means of observation. Hints of polarization already exist, as Van der Tak et al. observe polarization by scattering at centimeter wavelengths of Saturn's rings.[17] Submillimeter polarimetry should provide new information on particle sizes.

1.6 Experimentation Method:

We observed Saturn with SHARP from 2006 to 2011 on various observation runs. Our final combined image is shown by Figure 7.

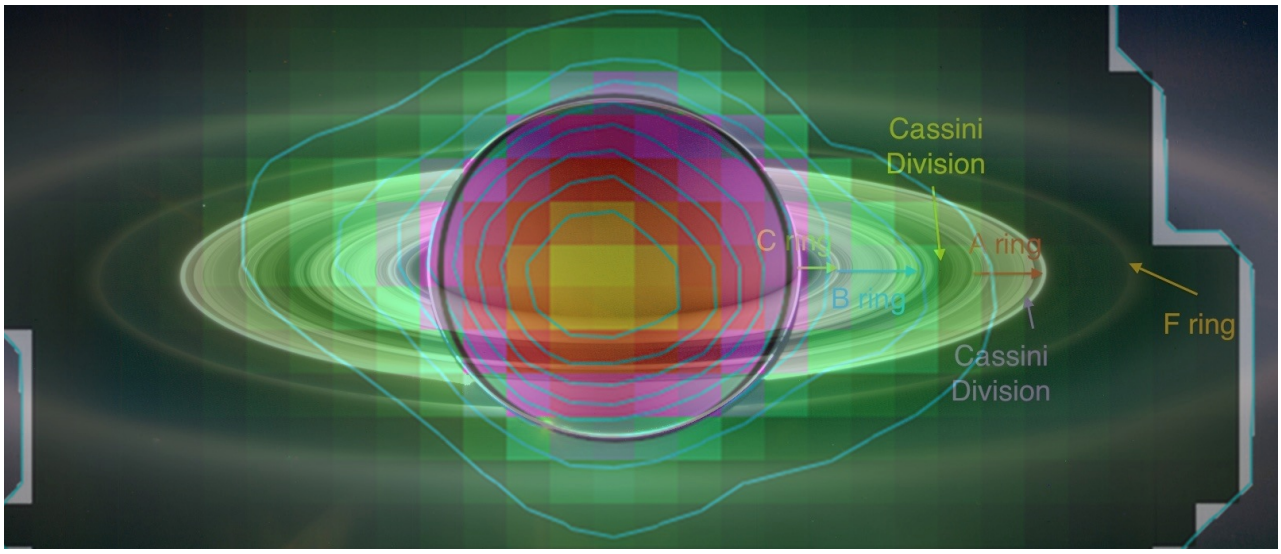

Figure 7: Overlapping polarimetry data with an image from Cassini 2007.

In Figure 7 above, my final result is overlapped with an image of Saturn and the classification of its rings from an image taken by Cassini. The light blue contour around Saturn in the figure is the 90% contour of intensity—90% of the intensity of the entire map lies within those lines. The F-ring is too dim to be analyzed, so we focus on the B-ring.

[16] Hedman, M.M., et al. 2011. The Christiansen Effect in Saturn's Narrow Dusty Rings and the Spectral Identification of Clumps in the F Ring. Icarus 215: 695-711. 706.
[17] Van der Tak, et al. 138.

I can restrict my analysis to the following 14 pixels outlined in yellow in Figure 8. In order to detect polarization from Rayleigh scattering alone, we narrowed our analysis to the ansae of Saturn's rings, or the side edges of Saturn's rings from our point of view (as suggested by Figure 9).[18] These 14 pixels, when compared to the overlapping image, correspond to the particles in the B-ring. Thus my analysis focuses on polarization by particles in the B-ring.

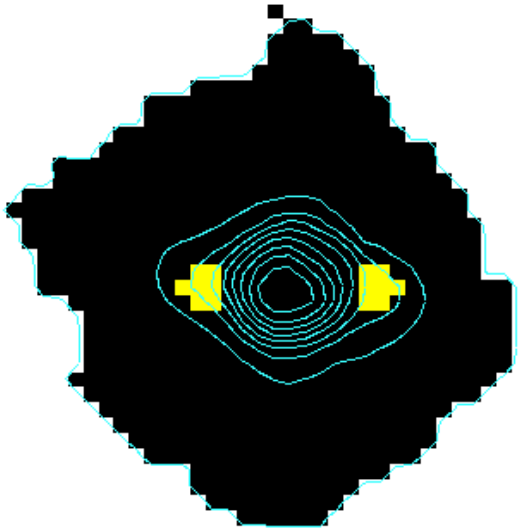

Figure 8: Restricting analysis to the B-ring.

In this specific region of the ansae, Rayleigh scattering is the only scattering mechanism observable from Earth. Because the incident light waves into these regions originate from the thermal emission of Saturn itself (shown by the blue arrows), Mie scattering within these side regions is not detectable from our perspective. It would be forward scattered to the left and right of this image. Since any detection of polarization within this region must be from Rayleigh scattering, these observations will give us information about the size of particles within the rings of Saturn. Using equations that relate particle size to Rayleigh scattering efficiency, we can estimate the particle size distribution of submillimeter-sized particles.

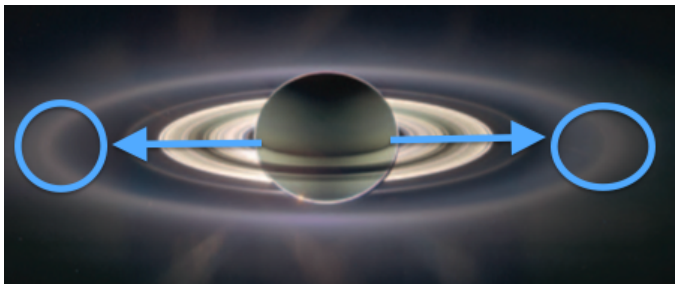

Figure 9: Picture of Saturn in eclipse. Polarization observed in the circled regions is only due to Rayleigh scattering, not Mie scattering. Incident light into circled regions are given by blue arrows.

[18] Esposito, 385.

By arguments made in section 1.3 (see Figure 4), we expected to see mostly vertically polarized light. The incident unpolarized light comes from the body of Saturn, interacts with the particles within the rings, and scatters radiation in our direction of observation that is vertically polarized. To give a quantitative prediction, we expected a +Q measurement of Stokes parameters in the ansae of Saturn's rings, which I will explain in the sections to follow.

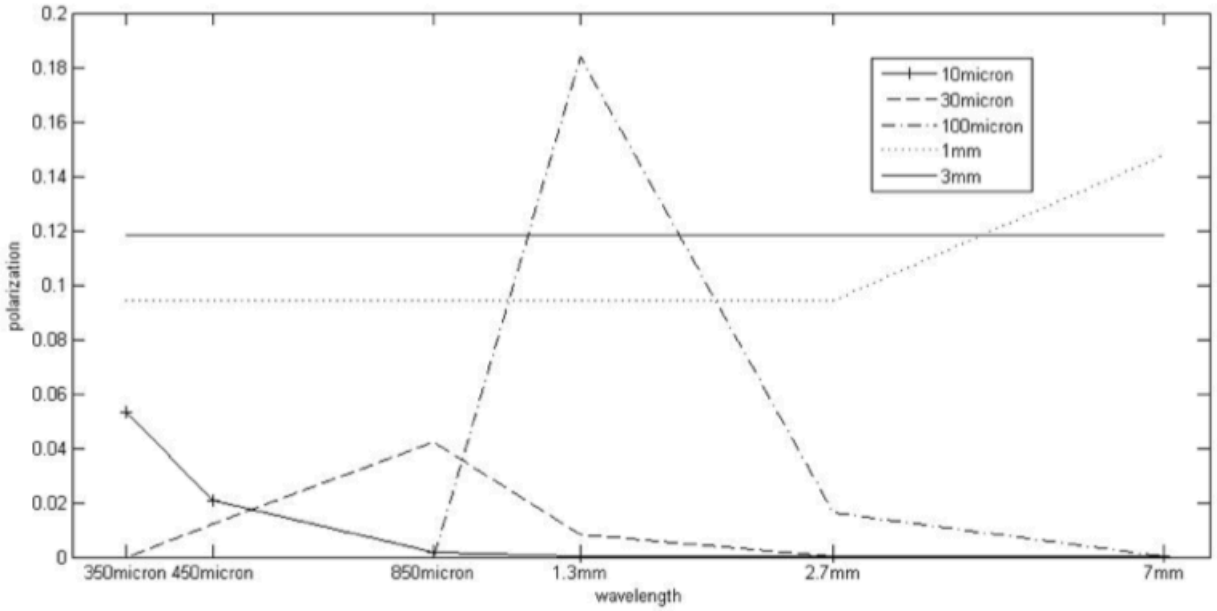

Figure 10: Observation of Polarization by Rayleigh scattering at different wavelengths with varying particle size.

In her PhD thesis, Megan Krejny analyzed scattered polarization due to different sized particles, as seen in Figure 10.[19] I hope to offer new evidence of polarization by small particles with actual data rather than the simulated data above. Referring back to my original goal, determining the particle size distribution of Saturn's rings will help establish the origins of such particles. This project will also provide a first example use of submillimeter polarimetry by Rayleigh scattering. In the future, this technique will be applicable to planet-forming disks and other T Tauri systems.

[19] Krejny, M. 2008. The Hertz-VPM Polarimeter and Applications of Multiwavelength Polarimetry. Ph.D dissertation, Northwestern University. 108.

Chapter 2: Stokes Parameters:

Accomplishing a quantitative analysis of polarization can be tricky. Take for example vertically polarized light, which oscillates up and down from the perspective of the viewer. One would think that adding polarization measurements is a simple vector summation, but the arithmetic is not so simple. Manipulating polarization "vectors" and attempting to use arithmetic methods for analysis is very tricky for several reasons. First of all, it is a misnomer to label polarization as "vectors," as a vector implies a specific direction. But in the case of vertically polarized light, it makes no sense to say that it is a vector in the up-direction, as the down-direction is equivalent. These polarization "vectors" experience symmetry over an angle of π. In this "vector" space, up is equivalent to down, left is equivalent to right, north-east is equivalent to south-west, etc. Furthermore, superposition of these vectors induces interesting phenomena. When adding these "vectors" in an incoherent fashion—meaning with a random distribution of phase differences—we obtain completely unpolarized light by overlapping vertically polarized light with horizontally polarized light. Similarly by overlapping diagonally polarized light with the opposite diagonally polarized light, we also obtain unpolarized light. To simplify this unorthodox algebraic structure, we use Stokes Parameters, first invented by George Gabriel Stokes.

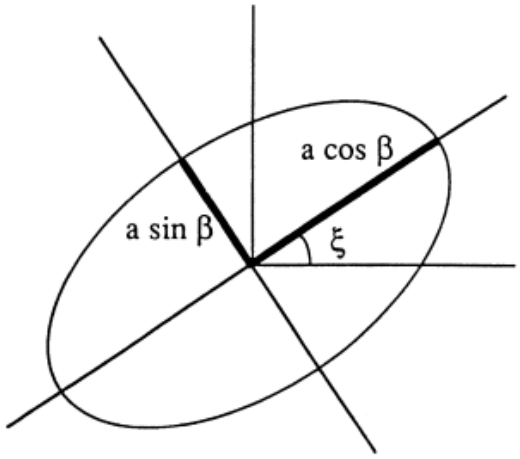

Figure 11: Elliptically polarized light as viewed from some frame of reference.

Consider the general polarization ellipse given by Figure 11.[20] The polarization is elliptical with semi-major axis $a\cos\beta$ and semi-minor axis $a\sin\beta$. The angle ξ is the angle between the semi-major axis and the x-axis of the reference frame. Then define the four Stokes parameters:

$$I = a^2$$
$$Q = a^2\cos 2\beta\cos 2\xi$$
$$U = a^2\cos 2\beta\sin 2\xi$$
$$V = a^2\sin 2\xi$$

[20] Hildebrand et al.,1222.

The I parameter corresponds to the intensity of the signal, and the other parameters are the magnitudes of polarization in different orientations. To understand what these transformations do intuitively, observe how vertically polarized light is transformed.

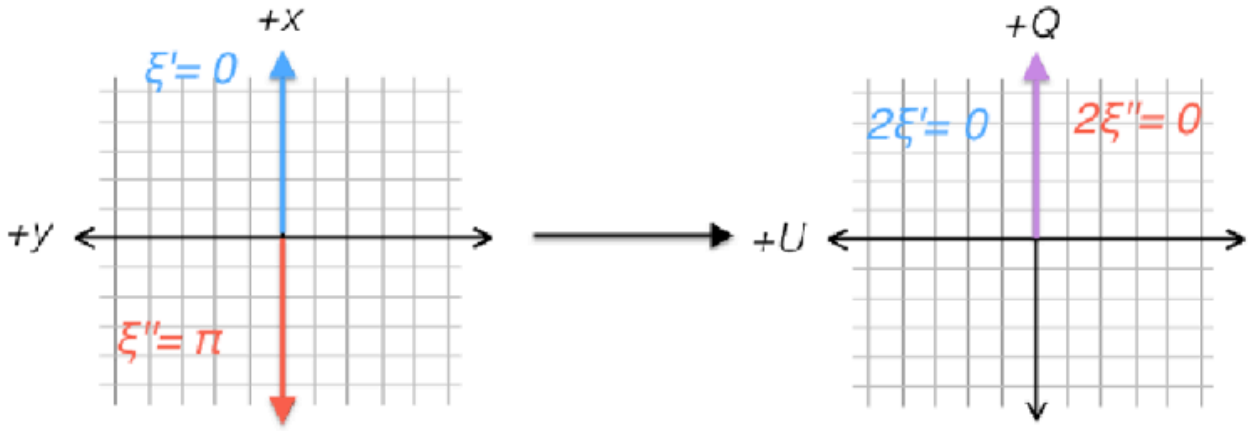

Figure 12: Transformation of vertically polarized light into Stokes space.

I have drawn vertical polarization as two "legs" with different angles. In this case, $\beta = 0$. Thus by rotating the top leg by $2\xi'$ and the bottom leg by $2\xi''$, we can see that they both transform to the same position. In this Stokes space where an angle ξ in real space corresponds to 2ξ in Stokes space, taking sine and cosine of this angle of $2\xi = 0$ concludes that vertical polarization corresponds to the +Q parameter.

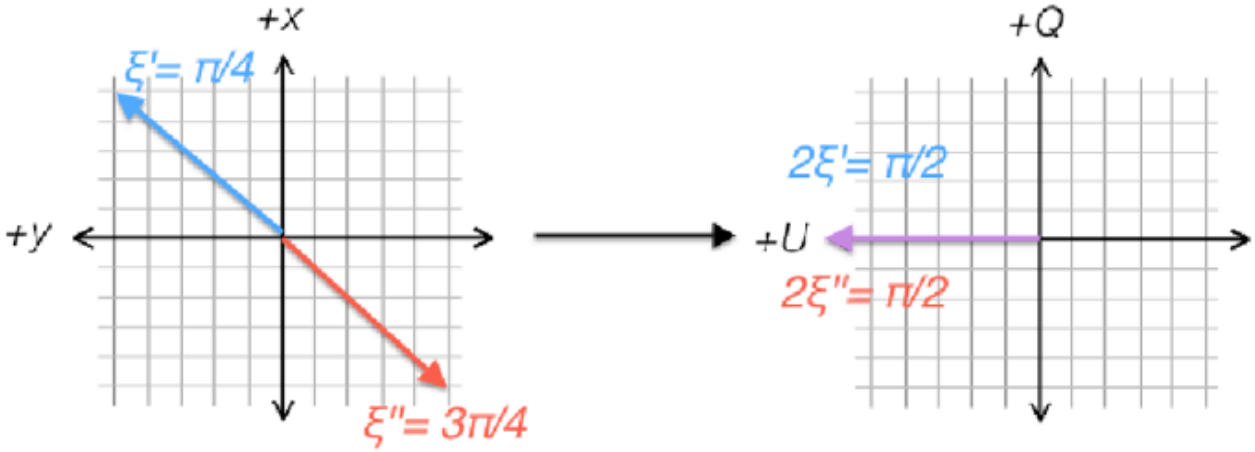

Figure 13: Transformation of diagonally polarized light into Stokes space.

Similarly, observe this diagonally polarized light. Again, the two "legs" transform to the same vector in a 2θ space. Taking sine and cosine of this angle $2\xi = \frac{\pi}{2}$, we get that this diagonally polarized light corresponds to the +U parameter.

By working through thought experiments to the other polarization signals, we get the following relations of Strokes parameters to the polarization signals in real space.

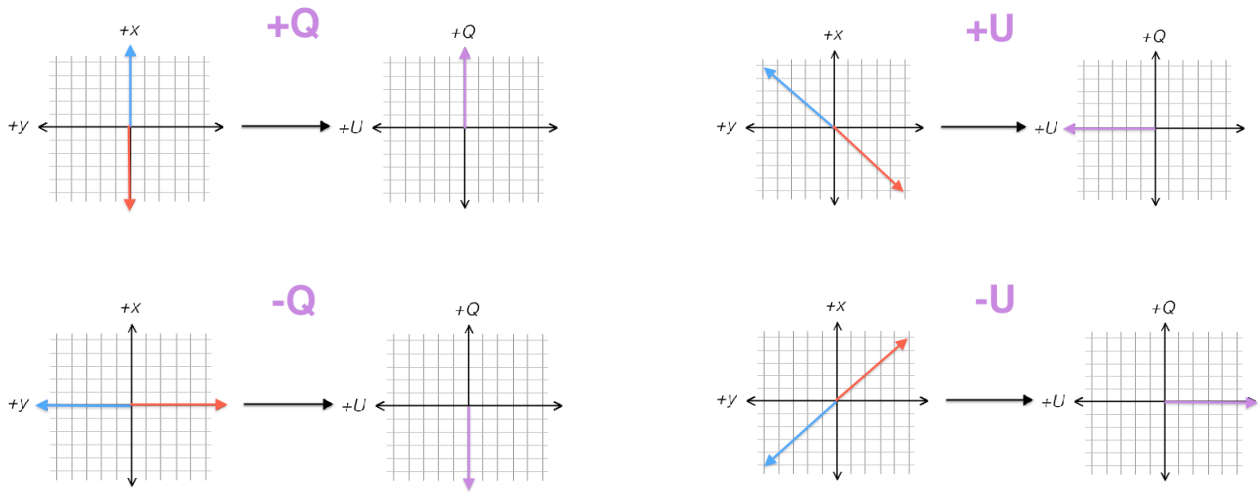

Figure 14: Strokes Parameters and their polarization orientations in real space.

We only measure linear polarization with SHARP, so we will not consider the circular polarization signals ± V. The reason why we do these arithmetic transformations is because superimposing polarized light is as simple as adding Stokes parameters. As stated before, superimposing vertically polarized light with horizontally polarized light gives unpolarized light. In terms of Stokes parameters, this means $(+Q) + (-Q) = 0$. Similar arguments are made for diagonally polarized light, or $(+U) + (-U) = 0$. The algebra of polarization "vectors" is immensely simplified when using Stokes Parameters.

Notice that by these definitions, for polarized light, we define Polarization P (when $V = 0$):

$$Q^2 + U^2 = I^2 P^2$$

Finally, define the normalized stokes parameters given by

$$q = \frac{Q}{I}, \; u = \frac{U}{I}$$

This results in the normalized definition of the fraction of light polarized as:

$$q^2 + u^2 = P^2$$

Chapter 3: SHARP:

3.1 Science:

Analysis of submillimeter polarization is the main objective of the SHARC-II Polarimeter (SHARP) research group at Northwestern University. The SHARP team is spearheaded by Professor Giles Novak, and focuses on mapping the Galactic magnetic fields to test theories of star formation. Within protostellar clouds, spinning non-spherical dust particles are observed to align their long axes with respect to the ambient magnetic fields. Because of this specific spatial orientation, the dust grains emit polarized light; the wavelength of this light is primarily in the submillimeter range due to the blackbody emission of dust particles at the low temperatures in protostellar clouds. Detection of submillimeter polarization thus reveals the direction of a cloud's magnetic fields, providing observations with which to test theories on star formation.[21]

Figure 15: SHARP module and the SHARC-II Camera at the Caltech Submillimeter Observatory.

3.2 Instrumentation:

The SHARP team at Northwestern University utilizes the Submillimeter High Angular Resolution Camera generation II (SHARC-II), mounted on the Caltech Submillimeter Observatory in Mauna Kea, Hawaii. SHARC-II is a 384-pixel submillimeter detector. For our specific purposes, we built the SHARP module, which is a stack of four boxes that lies between the CSO telescope and the SHARC-II detector. Figure 15 shows the four silver boxes of the SHARP module in front of the blue and gold SHARC-II camera.

[21] Attard, M., Houde, M., Novak, G., et al. 2009. Magnetic Fields and Infall Motions In NGC 1333 IRAS 4. The Astrophysical Journal 702: 1584-1592. 1585.

The SHARP module utilizes wire grid polarizers to split incident light into orthogonally polarized components. As can be seen by Figure 16,[22] unpolarized incident light that is transmitted through the wire grid becomes polarized because of the orientation of the wires. In the figure, the electrons within the wires are only allowed to oscillate in the horizontal direction, so the radiation emitted from these moving electrons cancels out the transmitted horizontal component from the incident light. This cancellation leaves only vertically polarized light to be detected.

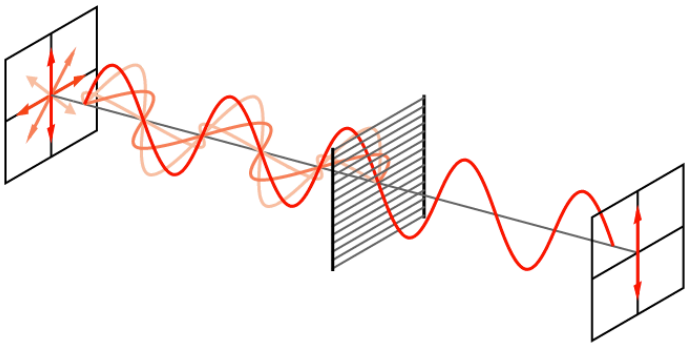

Figure 16: Wire grid polarizer interacting with unpolarized light.

In SHARP, the incident light enters the module, and the light is split into orthogonal directions of polarization with the help of a crossed grid. This crossed grid is comprised of two orthogonal wire grids, interlocked to separate the two components of polarization. Figure 17 shows the inner mechanics of the SHARP module of Figure 15, as it highlights the optical pathway for the photons. The light originates from the telescope, interacts with the crossed-grid at point A, is split into its horizontally and vertically polarized components as shown by the blue and green pathways, and then eventually focuses side-by-side in the SHARC-II camera.

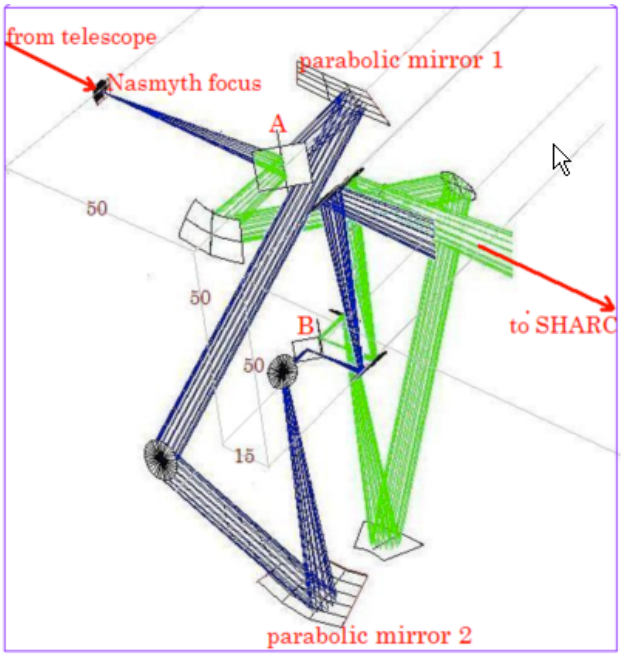

Figure 17: Optical pathway of observed light rays. Unpolarized light is decomposed into horizontal (blue) and vertical (green) components at the crossed grid located at position A.

[22] "Wire-Grid Polarizer." Wikimedia Commons. Web. 8 May 2013. <https://commons.wikimedia.org/wiki/File:Wire-grid-polarizer.svg>.

Thus the SHARC-II pixel array is effectively converted into two 12x12 side-by-side pixel arrays—shown by Figure 18.[23] We call these the H and V arrays, for horizontal and vertical polarizations respectively.

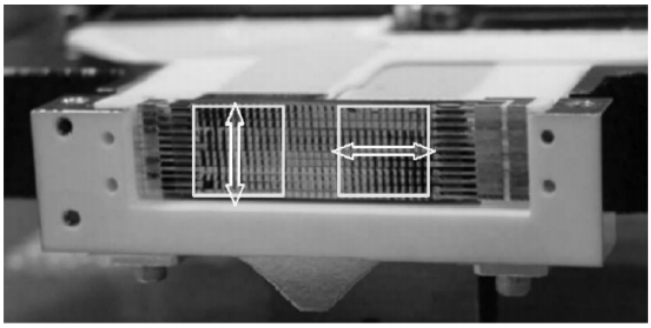

Figure 18: H and V pixel arrays in the SHARC-II camera. Each array detects one polarized component.

3.3 Half-Wave Plates:

As will be explained in the data analysis section later, making polarization measurements necessitates knowing how the polarization intensity varies as a function of the rotation angle. The rotation angle is the angle between the frame of the sky (with Celestial North pointing up) and the frame of SHARP (with up from the perspective of the camera pointing up), analogous in the example from section 1.2 to rotating a pair of sunglasses when looking at the blue sky. However, because the CSO telescope and the SHARP module are sturdy objects, rotating either of these is physically impossible. To work around this issue, we utilize a half-wave plate, which is a device that rotates incoming polarized light. As a brief explanation, refer to Figure 19.[24] The half-wave plate is a retarder; it specifically lags one incident wave. As the

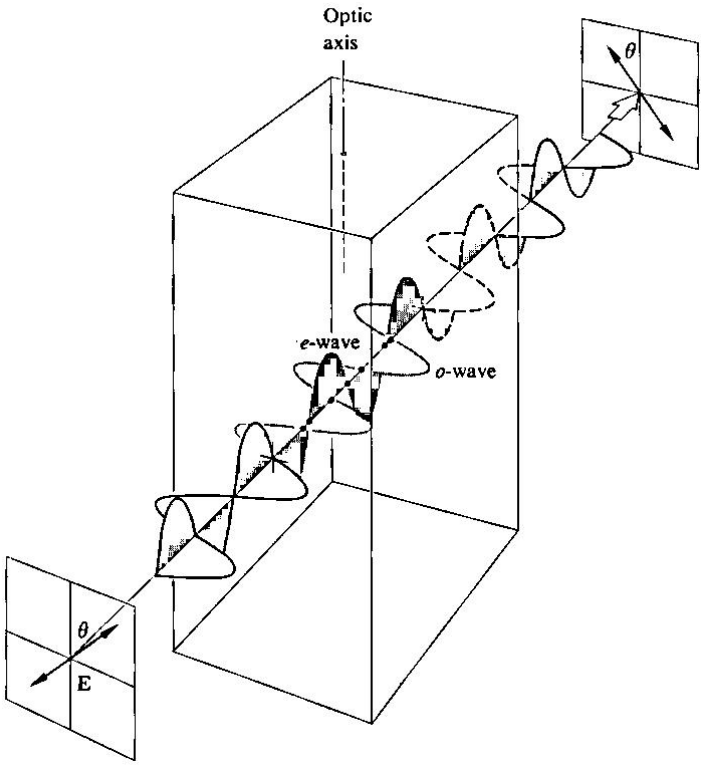

Figure 19: Half-wave plate changing the polarization of incident by retarding one orientation, but not the other.

[23] Li, H., et al. 2008. Design and Initial Performance of SHARP, a Polarimeter for the SHARC-II Camera at the Caltech Submillimeter Observatory. Applied Optics 47: 422-430. 423.
[24] Hecht, 348.

figure shows, the incident wave can be thought of as a composition of two orthogonal polarization signals: the e-wave and the o-wave, in the notation of Hecht's Optics. Half-wave plates function by allowing the e-wave to pass through unperturbed, but the o-wave lags behind by a certain phase. When the light wave exits the half-wave plate, the superposition of the unperturbed e-wave and the lagged o-wave result in a different polarization state. Though the mechanism may be complicated, the crucial idea is that half-wave plates alter the polarization angle of incident light waves.

By placing a half-wave plate before the crossed-grid in Figure 17 above, we can easily rotate a small half-wave plate before the polarizing grid, and this is a practical substitute for varying the rotation angle. At SHARP, we observe at 4 HWP angles: $\theta_{HWP} = 0°, 22.5°, 45°, and\ 67.5°$. These correspond to real rotation angles of $\theta_{real} = 2\theta_{HWP} = 0°, 45°, 90°, 135°$ in actual space. When taking these four measurements, we call it a "HWP cycle."

Chapter 4: Sources of Noise:

By the nature of observational astrophysics, astronomers are unable to create their own experiments. Astronomers must utilize clever processing techniques to acquire scientific substance from observations of existing sources. However, ground-based observation is extremely difficult, as astronomers are subject to atmospheric signals and noise pollution. As such, a significant portion of astronomical data analysis requires the separation of source signal and residual noise. For far-infrared polarimetry in particular, I will outline the different sources of noise and the methodology to combat them. Some methods utilize instrumentation techniques to minimize the noise, while others are determined analytically and subtracted from the data set. Thus I have defined two types of noise: noise that we correct for by instrumentation and mechanical schematics (Mechanical corrections) and noise that we must correct for by data analysis (Analytical corrections).

4.1 Mechanical corrections:

In order to understand the minimization of certain noises, I must first explain the process of chopping and nodding. As can be seen by Figure 21,[25] the source is at position "x" in the sky. However, the telescope points at a certain distance to the right of the source (between x and y_1). In this orientation, one of the mirrors in the telescope schematic—the secondary mirror— redirects the telescope focus to oscillate between point x and point y_1 with rapid repetition. We call this process "chopping" between x and y_1. In this position, we say x is in the "left beam" denoted "l" and y_1 is in the "right beam" denoted "r". After chopping nearly 100 cycles, the differences of the two $(l - r)$ are summed. The instrument then "nods" and switches the pointing to be at a point between x and y_2. Note that now y_2 is in the "left beam" and x is in the "right beam." Then the secondary

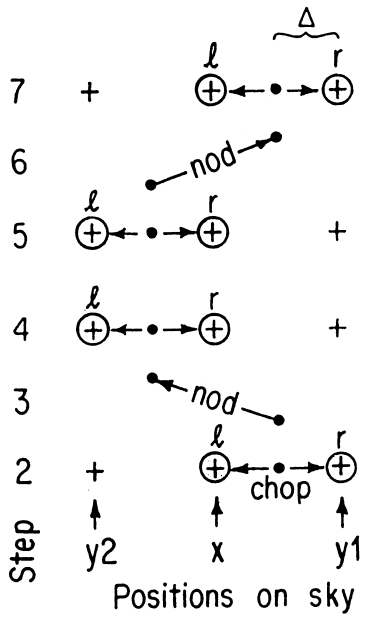

Figure 21: Chopping and Nodding. The off-centered telescope chops between two positions on and off the source, then nods to another off-center position.

[25] Hildebrand et al, 1218.

mirror again chops many times again between x and y_2, and this difference is summed as well. We say that one "chop-nod cycle" is when the telescope nods twice while chopping throughout, as Figure 21 denotes. After a single chop-nod cycle, we can acquire a measurement of our source by the following equation:

$$(l_x - r_{y_1}) - (l_{y_2} - r_x) - (l_{y_2} - r_x) + (l_x - r_{y_1}) = 4\left\{F(x) - \frac{[F(y_1) + F(y_2)]}{2}\right\}$$

In the above equation, l and r denote the "left" and "right" beams. $F(x)$ is the flux from the source, and $\frac{[F(\ _1)+F(y_2)]}{2}$ is the average flux off of the source, which we assume is approximately the background.

The reason why we utilize this chop/nod process at all is to minimize three noises: background noise, 1/f "sky" noise, and linear atmospheric gradients.

4.1.1 Sky Background Offset:

The background is the constant error that is due to constant emission of the atmosphere, external sources, electronic noise, or other constant noises. Because of their independent nature with respect to time, all measurements should measure similar error. Thus these constant sources of noise should be present in equal proportions within the flux of the signal, as well as the flux of the background. By subtracting out the background flux from the equation above, we rid the source signal of constant background noise.

4.1.2 "Offset" Gradients:

There may also exist linearly time-dependent atmospheric fluctuations that induce a linear noise distribution over the source. As Figure 21 shows, we nod twice in a single "chop-nod cycle" to end on the same position where we began. Ideally, the measurement from chopping initially and chopping in the same position after nodding twice should be identical. However a time-dependent gradient would cause a discrepancy between the two. Analyzing at both of these times gives us the ability to average the two and minimize any potential linear gradient, giving us a better representative of the background noise.

4.1.3 "Sky" Noise or 1/f Noise or Emission Noise:

The atmosphere is turbulent, and water particulates wander throughout the sky in a random fashion. Especially at submillimeter wavelengths, water particles emit radiation that contributes a significant amount of false signal in our measurements. These atmospheric fluctuations, which we call "sky noise," vary with time in an arbitrarily complex way. The "sky noise" is nearly 100,000 times brighter than the typical source. Ridding our data of "sky noise" is integral towards research.

This noise is similar to "random walk" statistics, and is relatively slow in its time dependence. If we denote this time-dependent noise as N(t), then taking the Fourier transform of the power spectral density of this noise gives us a function in the frequency domain $\widetilde{N}(f) = FT[N(t)]$.

Figure 22 is a logarithmic plot of the intensity of 1/f noise versus frequency.[26] We can see that the power of this noise in the frequency domain falls off by 1/f. If we can observe astronomical sources at fast enough frequencies, then the power of the noise falls to zero. So to rid this sky noise, we must chop at time scales much smaller than the fluctuation of the noise.

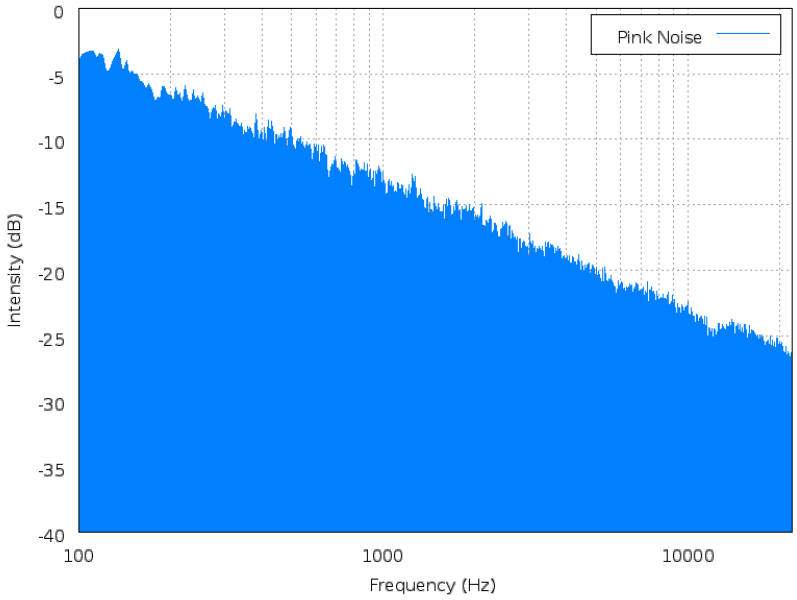

Figure 22: Logarithmic plot of 1/f noise.

To get a better understanding of chopping and nodding, observe the simulated 1/f noise below:

[26] "Pink Noise Spectrum." Wikimedia Commons. Web. 8 May 2013. <https://commons.wikimedia.org/wiki/File:Pink_noise_spectrum.png>.

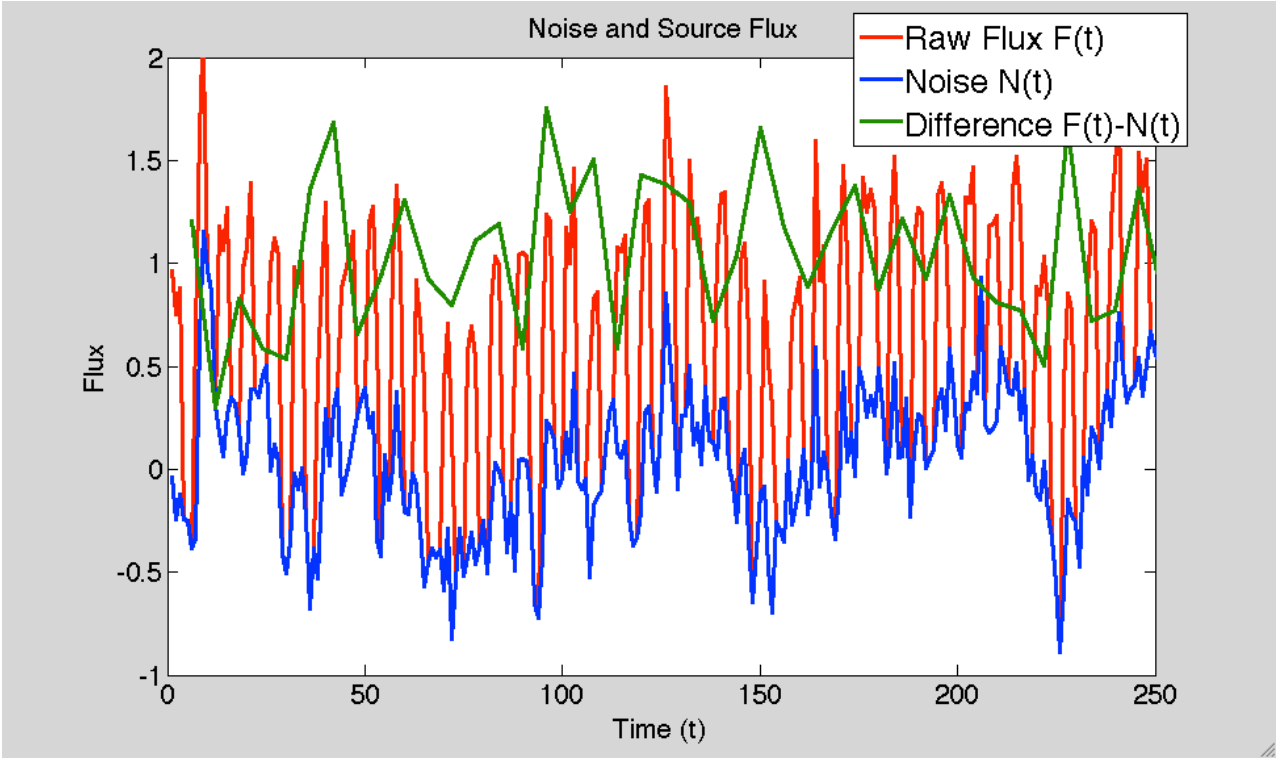

Figure 23: Simulated data of 1/f noise. With the noise given in blue, our raw signal of a source of flux 1 is given in red. Taking the difference gives the green curve.

Figure 23 is a plot of simulated 1/f noise in blue, along with a source of flux value 1. Because of the oscillating nature of chopping on and off the source, the raw flux in red oscillates along the time-dependent noise. If the chopping frequency is small enough, then the noise N(t) denoted by the blue line is relatively stable between a single chop. We can eliminate a portion of the sky noise by taking the difference at such small time scales, which is given by the green line. As can be seen, the green line wavers about the value +1, the flux of the actual source, but there still exists some amount of noise due to the time-dependence of 1/f noise. For SHARP, the chopping frequency is about $f \sim 1\,Hz$.

Chopping and nodding, though, does not completely extinguish this "sky" noise that has arbitrary time dependence. To rid as much residual emission and transmission noise from the sky, we utilize another method.

4.1.4 Transmission Noise:

Closely related to emission noise, incident light passing through Earth's atmosphere also must be transmitted effectively. If the absorptivity described by emission noise has arbitrary dependence on time, then the transmission efficacy also has a complex dependence on time. Thus this variation in transmission of light through Earth's atmosphere and the foreground must be accounted for.

To combat both of these noises, we utilize the fact that both emission and transmission noise are unpolarized, so both are present in the orthogonal directions of polarization. Thus, by separating the incoming polarized signal into the orthogonal polarization arrays H and V, both of these arrays exhibit the same time-dependent noise.

Since H and V are observed simultaneously, both the emission and transmission noise should be exactly the same in both H and V arrays. Thus, subtracting the flux from these arrays should eliminate this noise. Taking H-V minimizes the error due to arbitrarily complex time-dependent emission and transmission noise. Because this "sky" noise is very large in magnitude compared to our source signal, we incorporate this method to extract as much source signal as possible.

As the Figure 24 shows,[27] the individual pixel arrays (denoted in the figure as R, reflected, and T, transmitted, as opposed to our H and V arrays) experience arbitrary noise. The top two plots are for the R and T arrays separately, while the third plot shows the difference of the two. In the top two graphs, the data points shown by dots

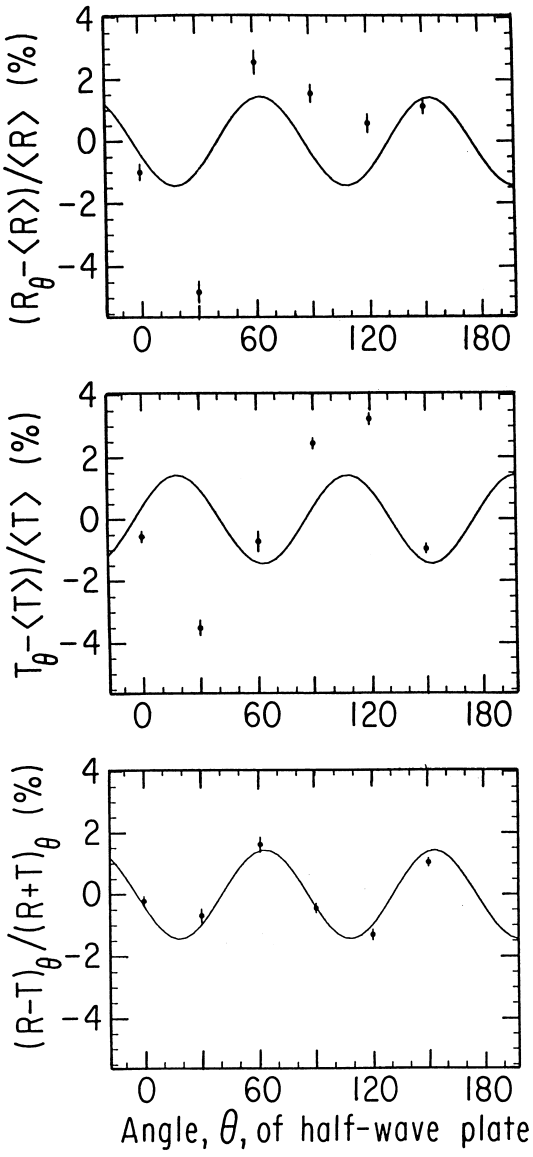

Figure 24: Differencing pixels arrays throughout one HWP cycle.

[27] Hildebrand, et al. 1221.

are distributed in the plot in almost a random fashion. The trigonometric curve in the middle shows the predicted values of polarization as a function of half-wave plate angle. The first two plots do not correlate well with the prediction. However the difference of the two in the bottom image shows that the observed data follows predicted values when subtracting the arrays, eliminating as much emission noise and transmission noise as possible.

4.1.5 Photon Noise or Shot Noise:

However, after all of these mechanical corrections, there still exists one very fundamental error. Due to quantum fluctuations, sources do not emit a constant stream of photons. Sources emit wave packets, which have a random distribution of photons per unit time. Thus, by the uncertainty principle, we cannot know the exact number of photons received per unit time, we can only find its expectation value (or mean). When we consider only the expectation value, there is still residual data for which our process either underestimates or overestimates. This is the fundamental photon noise due to quantum fluctuations, and its removal is impossible.

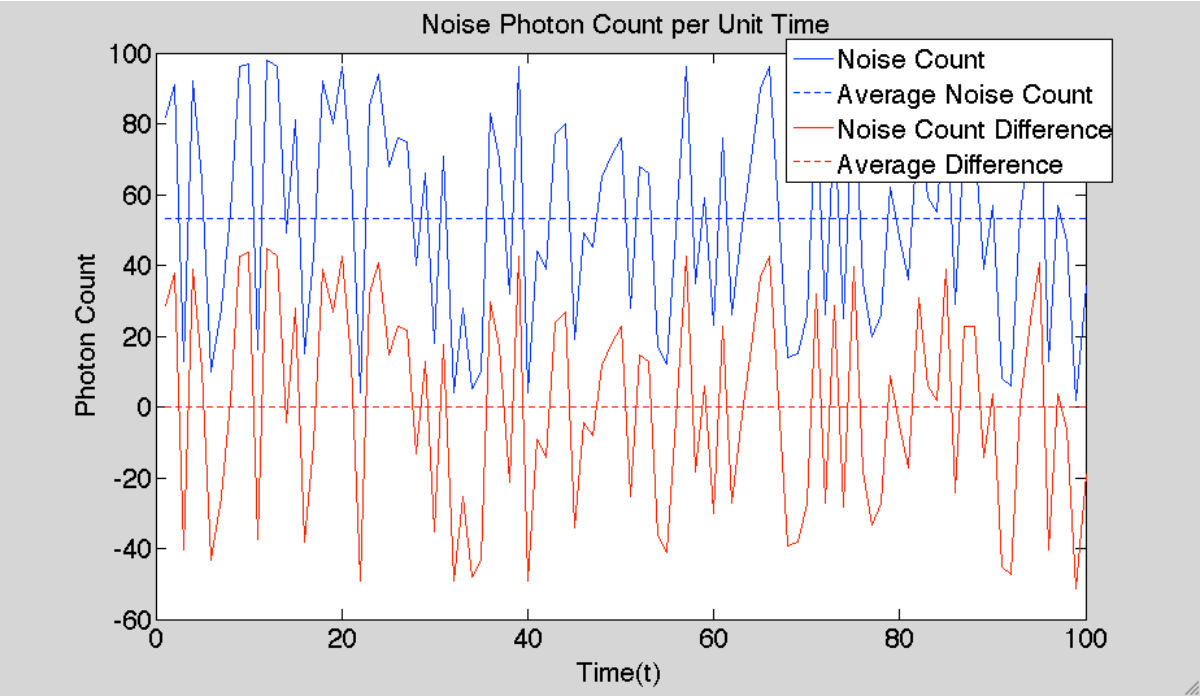

Figure 25: Simulated photon noise. By subtracting the average of photon noise, we are still left with an inherently noisy signal given by the red curve.

Figure 25 is a simulated plot of photon noise. The blue line gives the photon count of noise flux as a function of time, with its expectation value plotted in dotted blue. We can subtract this value from our data set, which gives the red curve. This red curve has a noise expectation value of zero, but at any given time, the actual noise is either above or below zero. Thus our final signal does still experience this fundamental noise as a function of time. This noise, however, dwindles down by a power of $\frac{1}{\sqrt{t}}$. After long periods of time, the average of the noise approaches zero. So by taking data over many days, we can only hope that our signal from the source is of magnitudes much larger than the photon noise, so that the photon noise is negligible.

4.2 Analytical Corrections:

By nature of instrumentation, systematic errors are introduced in our data that can be corrected for by data analysis.

4.2.1 Pointing or Drifting Error:

Because the telescope focus is imperfect, the calibration accuracy occasionally deteriorates. The telescope does not point exactly at locations of x, y_1, or y_2. To correct for this drift, one of our programs "fitgauss" analyzes our images, determines which pixel has the maximum intensity, and labels that pixel to be the center of the source. The pointing errors are then corrected by another program "sharpcombine," which reassigns the center pixel of the image.

4.2.2 Instrumental polarization:

Polarization can be due to the instrument itself. By utilizing the additive nature of Stokes parameters, we know that after all of the above noise corrections, our final polarization signals can be decomposed as

$$q_i = q_s + q_t + q_p$$
$$u_i = u_s + u_t + u_p$$

The polarization signal is due to three components: the source, telescope, and polarimeter (aka SHARP).

In order to understand the nature of these noises, we must understand the schematic of the CSO telescope and SHARP. Compare Figure 26 to Figure 11 above for the locations of SHARP, SHARC-II, and the telescope. Figure 26 depicts the CSO observing directly overhead, at elevation $e = 90°$.[28] Light comes directly down, reflects off the primary mirror, focuses onto the secondary mirror, reflects off of the M3 plane mirror, and enters SHARP.

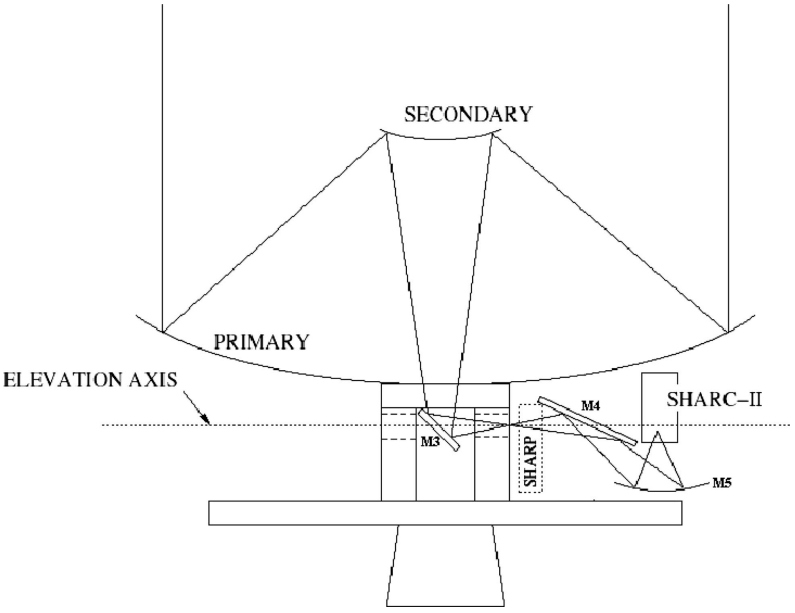

Figure 26: Schematic of the CSO telescope. The M3 mirror in the center of the telescope induces a polarization of $+q_t$.

Telescope Polarization:

Imagine the situation of the CSO observing the horizon at elevation $e = 0°$. Let q_t' and u_t' be the polarization due to the telescope specifically at this elevation of $e = 0°$. We expect equal portions of $+u_t'$ and $-u_t'$, so u_t' must average to be zero, which we constrain. However by the orientation of the mirror, we expect there to be an induced polarization of $+q_t'$. As Figure 27 shows,[29] polarization by reflection occurs and is only in the orientation that is orthogonal to the plane of incidence, which is in the $+q_t'$ direction.

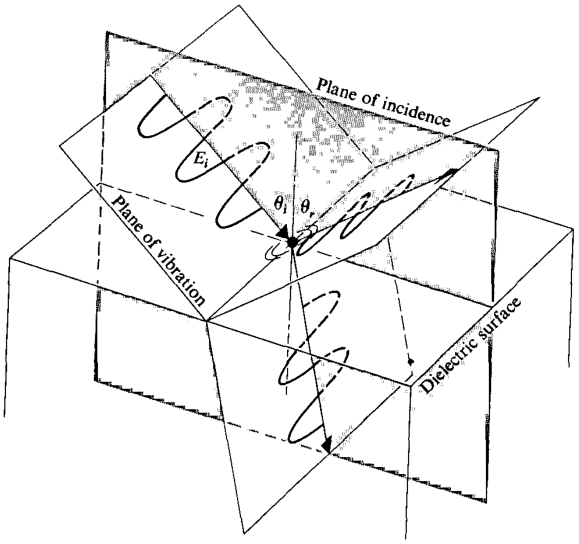

Figure 27: Polarization by reflection.

[28] Li et al., 423.
[29] Hecht, 344.

Once we find the instrumental polarization q_t' and u_t' at this specific elevation of $e = 0°$, we can find the polarization of the telescope at any arbitrary elevation. By raising the telescope to point at certain elevations, the M3 mirror rotates by an angle e as well. Thus the polarization due to the reflection should change as a function of elevation. To find the telescope polarization at any elevation, we can take this (q_t', u_t') vector and rotate it by an angle $2e$ (because Stokes space requires angles that are twice as large as the real angles). This gives the telescope instrumental polarization:

$$\begin{bmatrix} q_t(e) \\ u_t(e) \end{bmatrix} = \begin{bmatrix} \cos 2e & -\sin 2e \\ \sin 2e & \cos 2e \end{bmatrix} \begin{bmatrix} q_t' \\ u_t' \end{bmatrix}$$

Polarimeter Polarization:

After the signal is reflected off of the M3 mirror, it is processed in the SHARP module, which may induce more polarization errors. However in the frame of SHARP, this noise has no dependence on elevation and should be consistent in every signal.

By utilizing these different dependences on elevation, we can use clever data processing to determine both instrumental polarizations. First, we assume that the planets are unpolarized at submillimeter wavelengths.[30] So by analyzing the data from Jupiter, Saturn, and Mars, any polarization detected must be fake and attributed to telescope and polarimeter polarization. Because these planets have different elevations throughout each night, we can utilize this elevation dependence to separate the two instrumental polarizations as well. The telescope error should exhibit a dependence that looks analogous to trigonometric functions, but the polarimeter error is just a constant offset (as it is constant in every measurement).

Within this process of instrumental polarization, we used data taken from the planet of Saturn, and not the rings. By attaining the instrumental polarization from the instrument, we have not cancelled any polarization observed from the rings of Saturn.

[30] Li et al., 427.

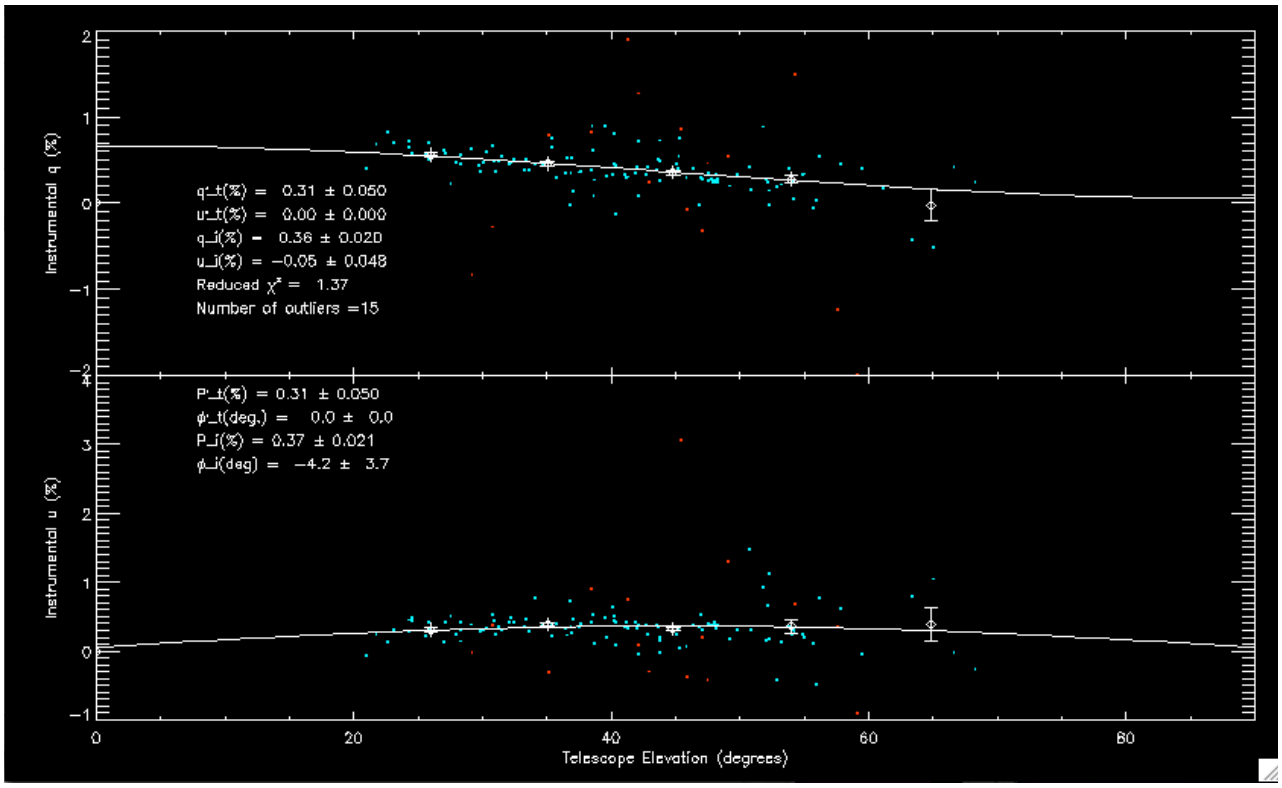

Figure 28: Instrumental polarization analysis of SHARP data from July 2006 to March 2009. The best-fit curves are trigonometric, corresponding to telescope polarization. The offset from zero is the polarimeter polarization.

I have analyzed all available data attained from July 2006 to November 2010 to determine the instrumental polarization corrections. At the CSO, the tertiary M3 mirror was resurfaced in September 2009, changing the instrumental polarization induced. Thus by plotting the data and using statistical analysis to verify its validity, I have attained the above plot. The data from planets are plotted in q and u. Their mean functions are plotted, which show trigonometric behavior that is offset from zero by a certain amount. Using the concepts described above, I have determined our errors due to the telescope itself.

At 350 microns for observations before September 2009,

$$q_p = 0.0034, \qquad u_p = 0.00017, \qquad q'_t = 0.00036, \qquad u'_t = 0.0$$

At 350 microns for observations after September 2009,

$$q_p = 0.0027, \qquad u_p = -0.0018, \qquad q'_t = 0.0001, \qquad u'_t = 0.0$$

For 450 micron runs, we use the ip values previously calculated

$$q_p = 0.0, \qquad u_p = 0.0, \qquad q'_t = -0.0015, \qquad u'_t = 0.0003$$

Once all of the errors described in this chapter have been accounted for, the data should be thoroughly processed for scientific analysis.

Chapter 5: SHARP Data Processing:

Before I explain the pipeline to process the Saturn-specific data, I will outline the pipeline to process data for the SHARP team in general. Overall, it requires three key steps: attaining single HWP cycle maps with "Sharpinteg," correcting drifting errors with "Fitgauss," and finally getting a single-run map with "Sharpcombine." After these steps, we obtain data files representing one image that describes an entire observation run — a single-run map.

5.1 Single HWP Cycle Maps:

Once the data files are chosen and organized, we run the files into a program named "sharpinteg." Sharpinteg processes the raw data files of a single HWP cycle and Relative Gain matrix (RGM) in order to output single-cycle maps. For each individual run, we process a large batch of files at once with the respective RGM file for that run. The RGM file is a simple table marking the relative sensitivities of each pixel to incoming photons. Thus, Sharpinteg scales the data acquired from each pixel accordingly.

As shown in Figure 14, the pixel array is separated into 3 sections, the H array, a middle portion that is not used, and the V array.

We combine the two V and H arrays into a new vector defined by

For i=[0,144] $signal_i = h_i - fv_i$

For i=[144,287] $signal_i = h_i + fv_i$

Where $signal_i$ is the signal of the i-th pixel, h_i is the signal of the i-th pixel in the H array,] v_i is the signal of the i-th pixel in the V array, and "f" is the relative gain between H and V. The difference in the first half of the vector is the signal with minimal noise that is used for analysis, while the sums in the second half of the vector are used later for normalization. We assume the relative gain is uniform, so we set $f = 1$ for data processing.

After all these relative differences are accounted for, Sharpinteg finally takes data from the HWP angles of $\theta = 0°, 22.5°, 45°, 67.5°$. Sharpinteg calculates the result of q_{raw} and u_{raw} by differencing these by the formulas:

$$q_{Raw} = 0.5[signal(\theta = 0°) - signal(\theta = 45°)]$$

$$u_{Raw} = 0.5[signal(\theta = 67.5°) - signal(\theta = 22.5°)]$$

At this point, we have processed a single cycle file, inputting data from 4 HWP angles and determining the raw signal.

5.2 Correcting Drifting Error:

Throughout the night, the telescope may lose calibration, causing the pointing errors described before. To correct for these drifting errors, “fitgauss” finds the coordinates for the Fixed Azimuth Offset (FAZO) and the Fixed Zenith Angle Offset (FZAO) to specify the center of the image. Since the center of the source may not be centered as time passes, we must determine how much the telescope has drifted. Fitgauss then determines the coordinates of the maximum intensity pixel in each file and records these results in a new text file “point.txt” to be used later. Also the atmospheric opacity tau must be corrected for 225 GHz, since tau varies as a function of the wavelength of light. Fitgauss also computes a smoothed tau for each file. Because the tau meter is noisy, work is done to produce high order polynomial fits to the data to create a smoothed tau for each night. These fits are available on the CSO website.

5.3 Single Run Maps:

Our program “sharpcombine” then inputs all of the single-cycle maps from a single run and interpolates them to acquire a final map. Sharpcombine takes in the point.txt file, which tells the program where the center of the source is, and interpolates the data relative to this center. In order to do this, the maps must be corrected for tau, the atmospheric opacity of the run. It also subtracts out the instrumental polarization from all pixels as detailed above. Then the map is rotated from the frame of the telescope to the frame of the sky, so that celestial north points in the up direction on the final maps. After all these corrections, sharpcombine interpolates the data to obtain the final single-run maps.

Chapter 6: Saturn Data Processing:

The data processing for Saturn data is very similar to that of the general SHARP pipeline.

6.1 Pre-Processing:

6.1.1 Determining Ring Plane Inclination:

Throughout the years, our view of Saturn is not always the same. Because we view Saturn at different parts of its and our orbit, we must be aware of how much of the ring we are able to see at any given time. With more ring visibility, we expected a large polarization signal from the ansae. Thus the ring visibility is a function of the ring plane inclination, which is the tilt of Saturn towards or away from our plane of view. As a resource, I have found an amateur astronomer's analysis of ring plane inclination as a function of time.[31] By plotting these values, I was able to obtain the following graph:

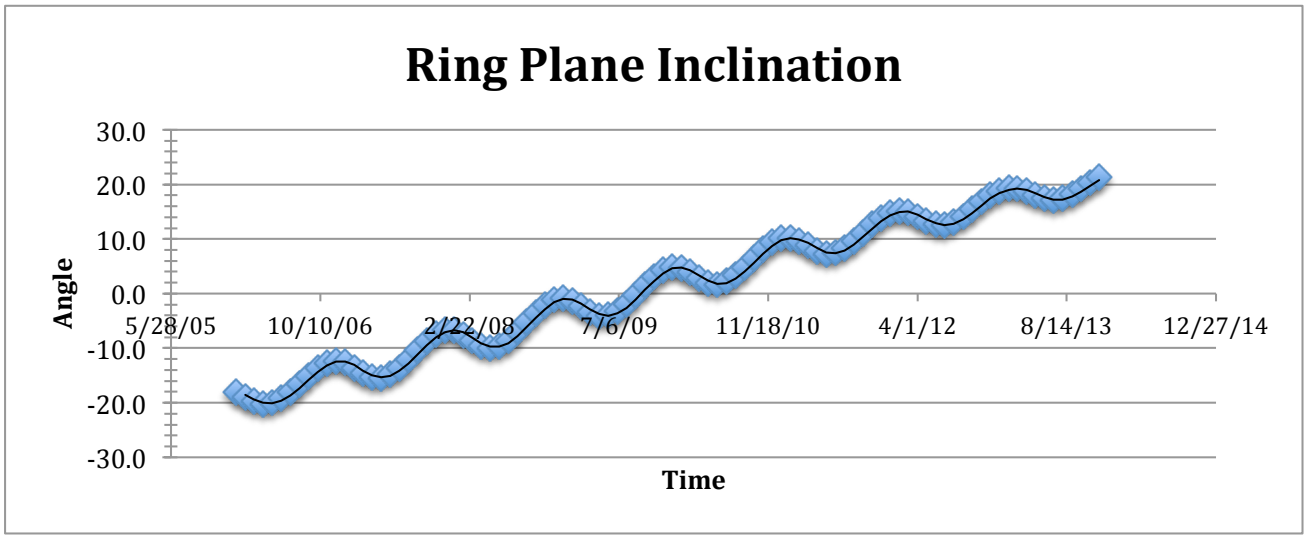

Figure 29: Data for ring plane inclination of Saturn's rings as a function of time, taken from an amateur astronomer.

I have visually checked these values with our data, and they are consistent.

[31] Kantelberg, R. 2013. "Ring-Plane Crossing." Astro-Imaging, 30 Mar. 2013. Web. 8 May 8, 2013.<http://www.astroimaging.com/Gallery/Solarsystem/Saturn/Ringplane/Ring_plane.html>.

6.1.2 Choosing Data:

As SHARP typically focuses on analyzing Young Stellar Objects, our data on planetary objects is scarce. SHARP only has polarimetry data for planets because of their use in instrumental polarization analysis. As a result, we only have Saturn data from a few observation runs. However, even then certain files are not available to be analyzed. About ten observation runs had Saturn data, but I was only able to analyze four runs, due to various complicated errors.

Observation Run	Error
2006 January	Processing in 2006 does not occur in HWP cycles. Pipeline is very different.
2006 December	Same as above.
2007 February	Chauvenet's criteria throws out all data.
2007 April	
2008 May	
2009 January	
2009 March	Saturn images were aborted.
2010 April	
2011 April	Chopper throw and nod length are not compatible.
2011 December	Only a single Saturn file was observed.

The data that I have used in my analysis are given below with their respective ring plane inclinations and initial HWP angle. The HWP angle is the offset from which the HWP rotates.

Observation Run	Ring Plane Inclination	HWP Angle
2007 April	$-15.4°$	$90°$
2008 May	$-7.0°$	$6°$
2009 January	$-1.2°$	$5°$
2010 April	$+2.4°$	$90°$

It is crucial to note that these runs were analyzed at 350 microns, except 2008 May, which was analyzed at 450 microns.

6.2 Processing:

At this point, processing the data is analogous to processing regular SHARP data. However, there is one extra step before running "sharpcombine." After running "fitgauss," the files must be processed by a program that changes its coordinates. The reason why we must input this step is because Saturn's coordinates of Right Ascension and Declination change substantially as a function of time. In typical SHARP data, our usual sources are so distant that changes in RA and Dec are negligible. However Saturn is relatively nearby and this approximation is not valid. Thus we set the RA and Dec of each image arbitrarily to $(45°, 30°)$, but any choice of numbers is valid. Now that the RA and Dec is similar, combining the single-cycle maps will not result in a blurry image.

These two images in Figure 30 plot the data from the 2009 January run. The first image is combined without first using this program. As can be seen, it is slightly blurrier than the right image. This blurry image bleeds the pink ring into the green region, so it appears unfocused.

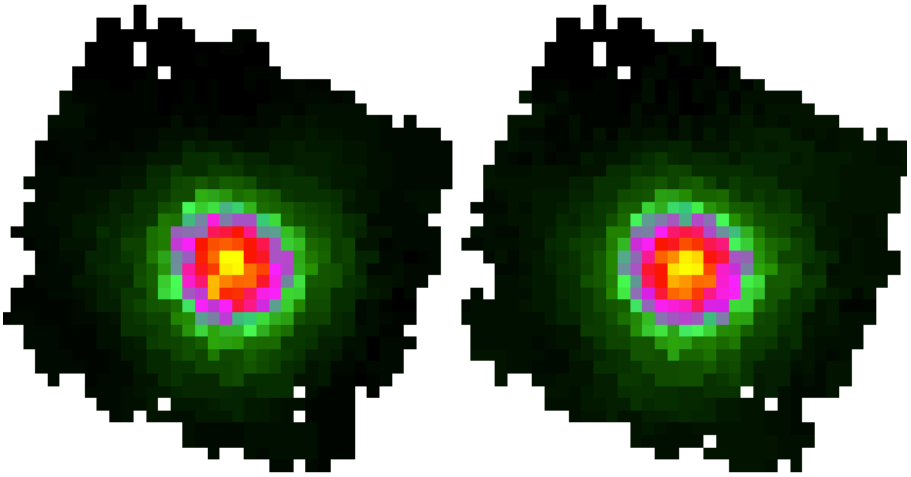

Figure 30: Processing Saturn first without changing (RA,Dec), giving the first blurry image. Processing again by changing (RA,Dec) gives a slightly clearer map.

After changing the coordinates, "sharpcombine" combines the files precisely.

At this point, we have obtained raw single-run maps for Saturn.

6.3 Post-processing:

6.3.1 Rotating North Pole:

After the processing pipeline, the four single-run maps (obtained from the four chosen observation runs) are oriented so that celestial north is always pointing up. These images are in the sky-frame. As a result, Saturn is arbitrarily rotated in this frame due to the geometry of both Earth and Saturn rotating around the Sun. This rotation makes it difficult to compare the polarimetry data, as similar values of q and u for different orientations of Saturn imply completely different results. We wish to rotate the images so that the direction of "up" in the image is along the direction of the north pole of Saturn.

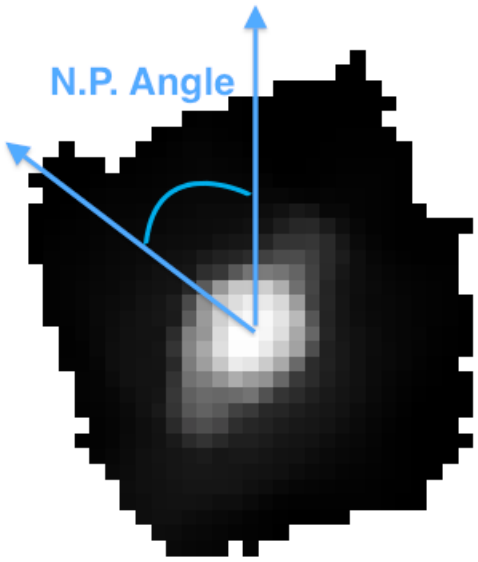

Figure 31: Definition of North Pole angle: the angle between the North Pole of Saturn and Celestial North.

In this Saturn-frame, the rings are horizontal and the two poles are aligned vertically.

The angles are obtained by using JPL's Ephemerides data for the North Pole Angle.[32] These angles are defined to be increasing counter clockwise starting at $0°$ pointing at Celestial North.

Observation Run	North Pole Angle
2007 April	$353.44°$
2008 May	$354.02°$
2009 January	$355.2161°$
2010 April	$354.83°$

Rotating an image by an angle θ corresponds to rotating the polarization "vectors" in Stokes space by $\xi = 2\theta$. The rotation matrix is given by

$$\begin{bmatrix} q_{rot} \\ u_{rot} \end{bmatrix} = \begin{bmatrix} -\cos 2\theta & \sin 2\theta \\ \sin 2\theta & \cos 2\theta \end{bmatrix} \begin{bmatrix} q \\ u \end{bmatrix}$$

[32] "HORIZONS Web-Interface." Jet Propulsion Laboratory – California Institute of Technology. Web. 8 May 2013. <http://ssd.jpl.nasa.gov/horizons.cgi>.

6.3.2 50% Intensity Offset:

We assume that the planets should be unpolarized at submillimeter wavelengths, as the mechanisms of emission do not imply polarized light.[33] This is the same idea that motivated our instrumental polarization analysis. By comparing our final maps, we do see slight polarization on the planet of Saturn. So by taking advantage of the notion of unpolarized planets, I have calculated the average values of pixels within the 50% intensity contour, and then subtracted these average values from the entire map. By accomplishing this offset, the final average of pixels within the 50% contour (approximately the disk of Saturn) for both q and u is zero.

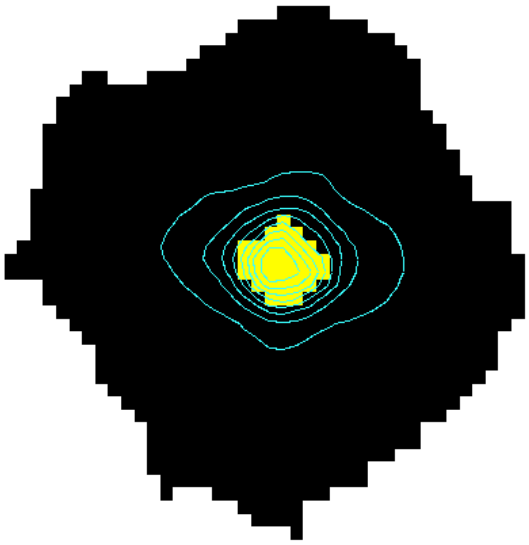

Figure 32: The disk of Saturn, within the 50% intensity contour.

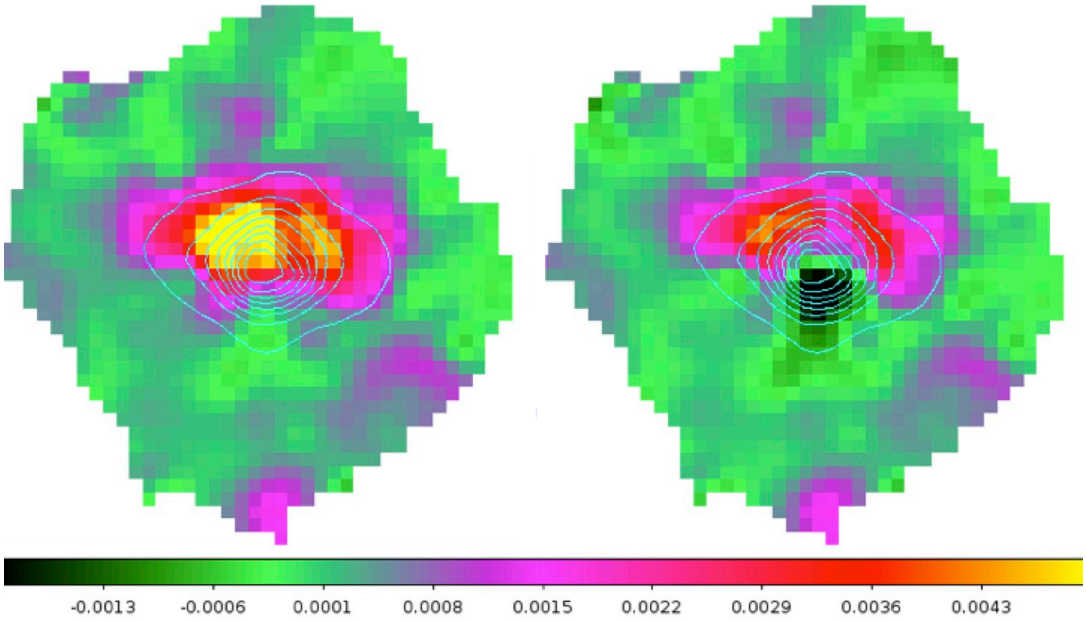

Figure 33: Single-run map of May 2008 showing the q parameter before and after completing the 50% contour offset.

[33] Li et al., 427.

6.3.3 Creating Intensity Contours:

For visualization purposes, it is important to plot the intensity contours. I have set each level to be 10% of the maximum intensity. Then I overlaid these contours on all images of q, σ_q, u, σ_u, etc.

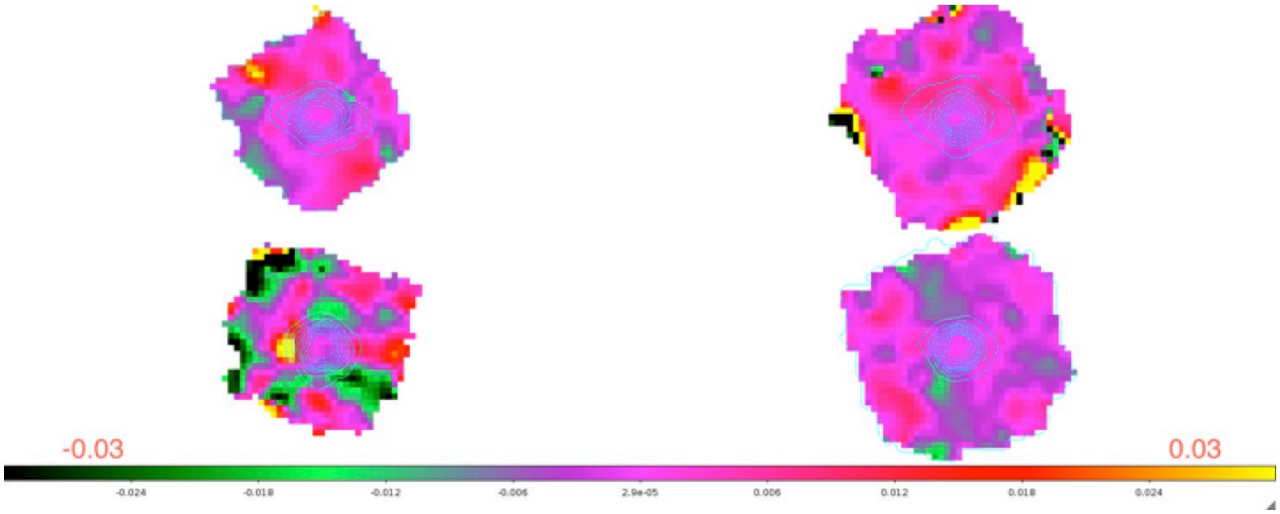

Figure 34: Final single-run maps showing normalized q parameter, all on the same scale. Read from left to right, top to bottom, the four images are: 2007 April, 2008 May, 2009 January, and 2010 April.

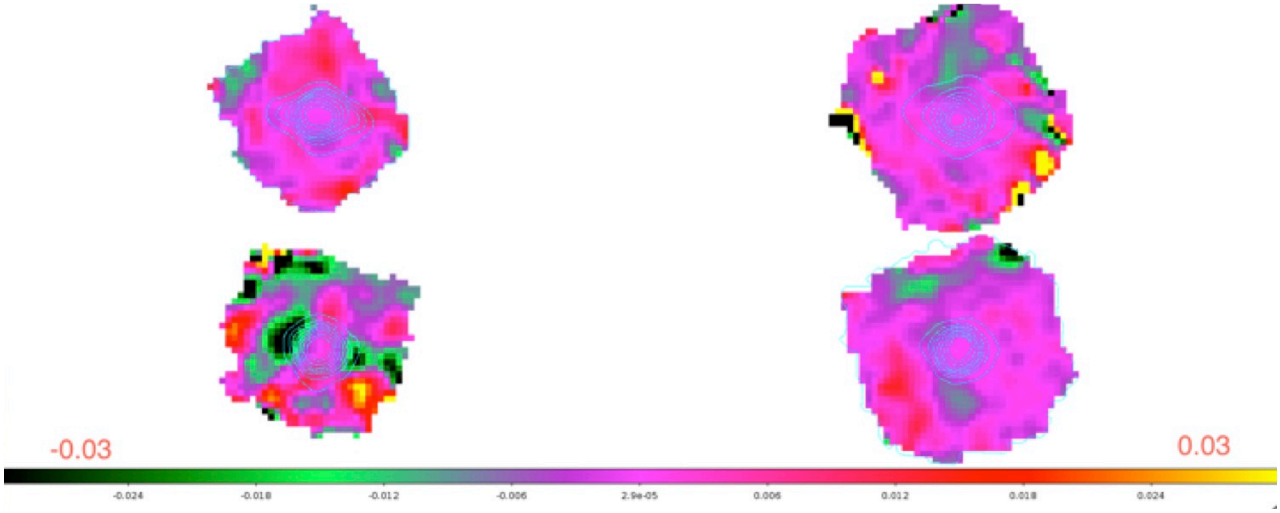

Figure 35: Final Single-run maps showing normalized u parameter, all on the same scale. Read from left to right, top to bottom, the four images are: 2007 April, 2008 May, 2009 January, and 2010 April.

6.3.4 Final Single Image:

To obtain a final single result, we combined our files once again to obtain a final Saturn map. At this step, we did not use 2009 January or 2010 April data, as their ring plane inclinations are too low —they are edge-on. These observational runs do not offer significant signal. We combined the April 2007 data with the May 2008 data because their ring plane inclinations were large enough for us to obtain data pertaining to Saturn's rings. In order to combine the files, I wrote a new program. I defined a new image that plots a pixel-by-pixel weighted average for each frame of q, σ_q, u, σ_u, etc.

$$Signal_i = \frac{1}{2}\left[\frac{Signal_i(2008\ May)}{Max_I(2008\ May)} + \frac{Signal_i(2007\ April)}{Max_I(2007\ April)}\right]$$

By doing this, we get the final image:

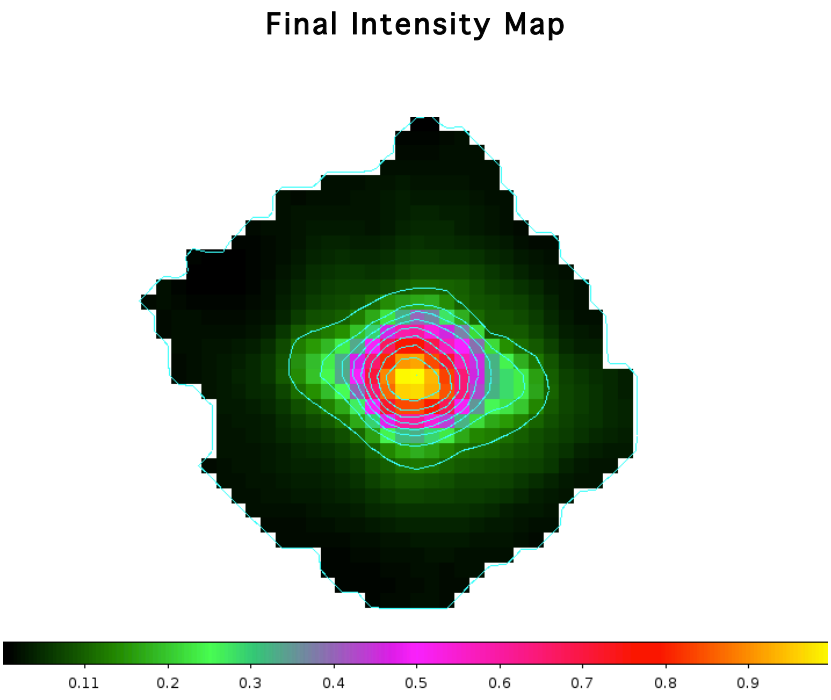

Figure 36: Final combined map of Saturn's intensity, using 2007 April and 2008 May data.

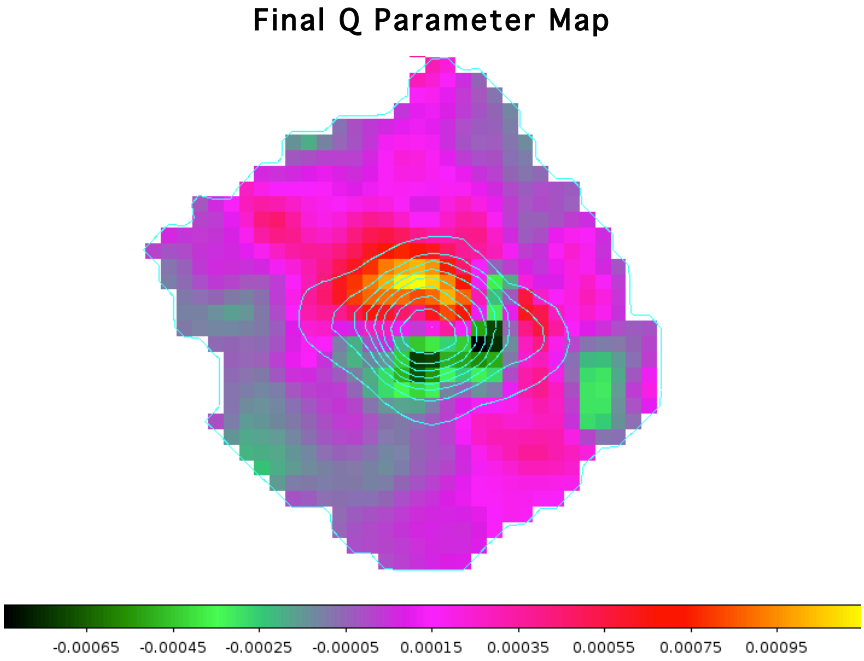

Figure 37: Final combined map of Saturn's Q parameter, using 2007 April and 2008 May data.

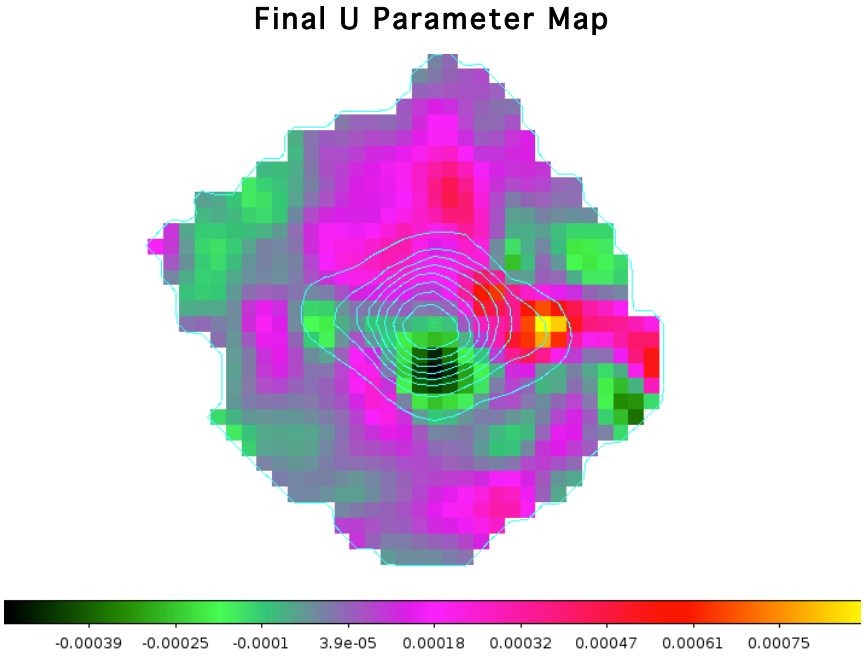

Figure 38: Final combined map of Saturn's U parameter, using 2007 April and 2008 May data.

6.4 Final Polarization Signal

After all of the Saturn data processing, we have finally obtained a single combined image that had interpolated every file from the 2007 April and 2008 May observation runs.

To obtain final quantitative values of polarization, we define the variables

$$I_{ansae} = < I >_{ansae} = \frac{\sum_{ansae} I_i}{\sum_{ansae} 1}$$
$$Q_{ansae} = < Q >_{ansae} = \frac{\sum_{ansae} Q_i}{\sum_{ansae} 1}$$
$$\sigma_Q = Q_{RMS}$$
$$U_{ansae} = < U >_{ansae} = \frac{\sum_{ansae} U_i}{\sum_{ansae} 1}$$
$$\sigma_U = U_{RMS}$$

These variables give average values of I, Q, and U of just the pixels in the ansae. The errors are defined to be the Root-Mean-Square of the entire map, as we assume the error of the whole map is similar to the error in just the ansae.

However, we must normalize the Q and U stokes parameters. Thus, the final values of q and u with their respective errors are defined to be

$$q_{ansae} = \frac{Q_{ansae}}{I_{ansae}}$$
$$\sigma_{q_{ansae}} = \frac{\sigma_{Q_{ansae}}}{I_{ansae}} \approx \frac{\sigma_Q}{I_{ansae}} = \frac{Q_{RMS}}{I_{ansae}}$$
$$u_{ansae} = \frac{U_{ansae}}{I_{ansae}}$$
$$\sigma_{u_{ansae}} = \frac{\sigma_{U_{ansae}}}{I_{ansae}} \approx \frac{\sigma_U}{I_{ansae}} = \frac{U_{RMS}}{I_{ansae}}$$

Finally, this gives us the values of

$$q_{ansae} \pm \sigma_{q_{ansae}} = 0.00074863279 \pm 0.0010155016$$
$$u_{ansae} \pm \sigma_{u_{ansae}} = 0.00097274407 \pm 0.00066649504$$

With the definition of polarization and the process of propagating errors,[34] we obtain

$$P = \sqrt{q^2 + u^2}, \qquad \sigma_P = \sqrt{\sigma_q^2 \left(\frac{\partial P}{\partial q}\right)^2 + \sigma_u^2 \left(\frac{\partial P}{\partial u}\right)^2 + 2\sigma_{qu}^2 \left(\frac{\partial P}{\partial q}\right)\left(\frac{\partial P}{\partial u}\right)}$$

Where $\frac{\partial P}{\partial q} = \frac{q}{\sqrt{q^2+u^2}} = \frac{q}{P}$ and $\frac{\partial P}{\partial u} = \frac{u}{\sqrt{q^2+u^2}} = \frac{u}{P}$. I am assuming $\sigma_{qu} = 0$.

Our final result is

$$P = 0.001227 \pm 0.0008164$$

I set an absolute upper limit of polarization as $P_{5\sigma_P} = P + 5\sigma_P = 0.005309 = 0.530\%$.

[34] Bevington, P., Robinson, D. 2002. *Data Reduction and Error Analysis for the Physical Sciences*. New York, NY: McGraw-Hill, Inc.

Chapter 7: Toy Model of Saturn's Ansae:

7.1 A "Toy Model" for Polarization of Saturn's Ansae:

With the upper limit of polarization at submillimeter wavelengths, we are now able to discuss the implications of this result. As the previous section shows, we have set an upper limit at $P_{5\sigma_P} < 0.530\%$ by observing Saturn at 350 and 450 micron wavelengths. For the analysis of this measurement, we will average the two and say this polarization corresponds to first approximation to observing at a 400 micron (0.4 mm) wavelength.

As mentioned in the introduction, one motivation for this project was that Van der Tak et al. observed significant polarization with the Very Large Array (VLA) at radio wavelengths. At 3.6 cm, they measured $P(3.6\,cm) = 31\% \pm 10\%$, while at 6.1 cm, they measured $P(6.1\,cm) = 35\% \pm 10\%$.[35] Van der Tak et al. attribute this polarization to Rayleigh scattering by centimeter size particles.[36] Compared to our limit $P(0.4\,mm) < 0.530\%$, the radio wavelengths exhibit significantly more polarization than the submillimeter.

Esposito mentions that particles in Saturn's rings tend to range from the smallest size of 1 cm to the largest size of 20 meters.[37] However, recent literature mentions that the particle size distribution of Saturn's B ring is still unknown.[38] To attempt to explain the polarization measurements attained by us at SHARP and those at the VLA, we have created a crude "toy model" of the particles in Saturn's rings.

We consider four sizes of particles with different diameters: boulders ($d = 10\,m$), pebbles ($d = 0.01\,m$), large dust grains ($d = 1\times10^{-4}\,m$), and small dust grains ($d = 1\times10^{-5}\,m$). We assume that the only two polarization mechanisms are those of reflection and Rayleigh scattering, with one typically more dominant than the other depending on the size to wavelength ratio. Also because of differing particle sizes, the luminosity mechanisms may be slightly altered, as will be explained in the following sections.

By using this toy model, we attempt to estimate the number of particles of each size given by $N_B, N_P, N_L,$ and N_S corresponding to boulders, pebbles, large grains, and small grains respectively. By setting $N_B = 1$, our estimates will give the number of particles per boulder.

---

[35] Van der Tak, et al. 138.
[36] Van der Tak, et al. 146.
[37] Esposito, 386.
[38] Ferrari, C., Reffet, E. 2013. The Dark Side of Saturn's B Ring: Seasons as Clues to its Structure. *Icarus* 223: 28-39. 28.

To summarize the type of process treated for each particle, refer to Table 7.1. Because of the ratio of particle size to wavelength, which will be explained below, we must treat the luminosity and polarization mechanisms like so:

Particle Type	Luminosity Mechanism			Polarization Mechanism		
	0.4 mm	3.6 cm	6.1 cm	0.4 mm	3.6 cm	6.1 cm
Boulders $d = 10\ m$	Blackbody	Blackbody	Blackbody	Reflection	Reflection	Reflection
Pebbles $d = 0.01\ m$	Blackbody	Adjusted blackbody	Adjusted blackbody	Reflection	Rayleigh scattering	Rayleigh scattering
Large Grains $d = 1\times10^{-4}\ m$	Adjusted Blackbody	Adjusted Blackbody	Adjusted Blackbody	Rayleigh Scattering	Rayleigh Scattering	Rayleigh Scattering
Dust Grains $d = 1\times10^{-5}\ m$	Adjusted Blackbody	Adjusted Blackbody	Adjusted Blackbody	Rayleigh Scattering	Rayleigh Scattering	Rayleigh Scattering

Table 7.1: Experimental Method of different particle sizes and different wavelengths.

7.2 Index of Refraction:

The theory of scattering and luminosity require an understanding of the index of refraction. In typical physics texts, the refractive index of a medium is defined to be the ratio of the speed of light within that medium to the speed of light in a vacuum:

$$n = c/v$$

While useful in most situations, this definition is not adequate enough for our purposes. By incorporating a complex component into the refractive index, we can account not only for reflective properties, but also for absorptive properties. Thus we can define the complex index of refraction:

$$m = n + ik$$

However in this case as we will explain later in section 7.2.1, "n" is the real component of the refractive and no longer represents the ratio of light speeds, but they are still related. The imaginary component is denoted by "k" and is related to the conductivity of the material.

There exists an ambiguity in the sign convention of "k", depending on the field of research and the year of publication. Even within the sources used for this project, the notation varies. We will initially adopt a positive sign convention to determine the value, but then we will change it to negative to remain consistent with the theoretical work.

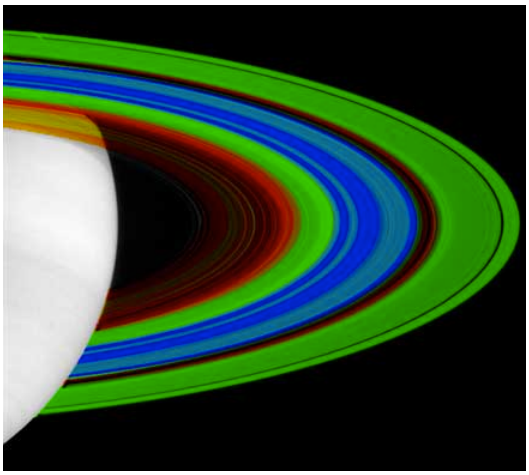

Figure 39: Temperature differences within Saturn's rings. The green portion, where the B-ring resides, corresponds to 70 K.

For our purposes, we must have an estimate of the complex index of refraction for the particles of Saturn's rings. Being an astronomical source, directly measuring the index is quite difficult. To make an estimate, we assumed that the particles were comprised completely of ice. [39] For our purposes, this approximation is nearly correct, but the reddish color of Saturn's rings does imply a slightly higher absorptive component than we account for. We also approximate the temperature of the B-ring to be roughly 70 K, as estimated by NASA.[40]

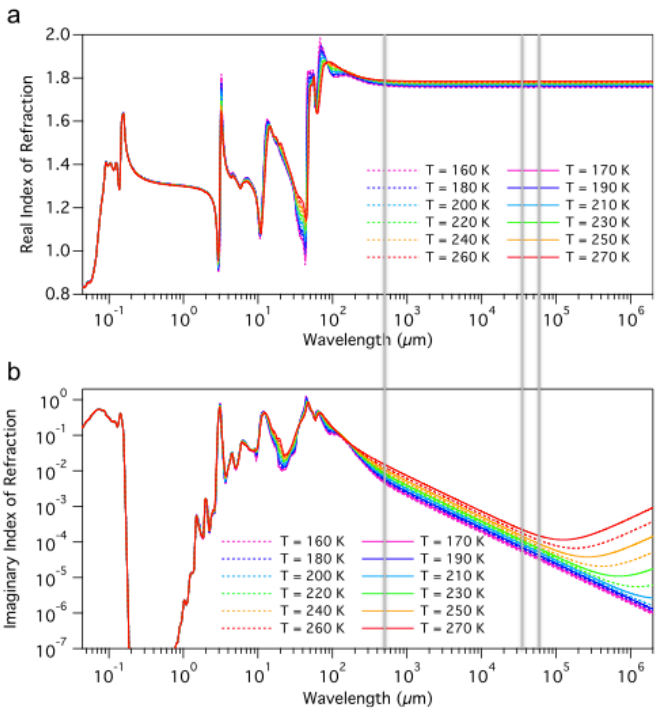

Figure 40: Temperature and wavelength dependence of the complex index of refraction. Gray vertical lines denote 0.4 mm, 3.6 cm, and 6.1 cm wavelengths.

Useful for spectroscopy analysis, these optical constants for ice have been estimated for various temperatures by Iwabuchi and Yang. [41] However, their estimates only account for temperatures in the range of 160 K to 270 K. As can be seen by Figure 40, both components of refractive index are wavelength and temperature dependent.

[39] Esposito, 387.
[40] Watanabe, S. 2008. "Saturn's Rings, Cold and Colder." NASA, 29 Apr. 2008. Web. 8 May 2013. <http://www.nasa.gov/mission_pages/cassini/multimedia/pia06425.html>.
[41] Iwabuchi, H., Yang, P. 2011. Temperature Dependence of Ice Optical Constants: Implications for Simulating the Single-Scattering Properties of Cold Ice Clouds. *Journal of Quantitative Spectroscopy & Radiative Transfer* 112: 2520-2525. 2522.

By analyzing data presented by Iwabuchi et al. pertaining to our specific wavelengths, fitting a linear plot to the real index "n" and an exponential plot to the imaginary index "k" gives us the approximate complex index of refraction at 70 K as

$$m(0.4\ mm) = 1.7469 - 0.0027033i$$
$$m(3.6\ cm) = 1.7364 - 0.000016675i$$
$$m(6.1\ cm) = 1.7364 - 0.000076111i$$

Note that for these indices, Iwabuchi et al. use the positive convention for the imaginary component "k." We have already changed it to the negative convention to be consistent with formulas later.

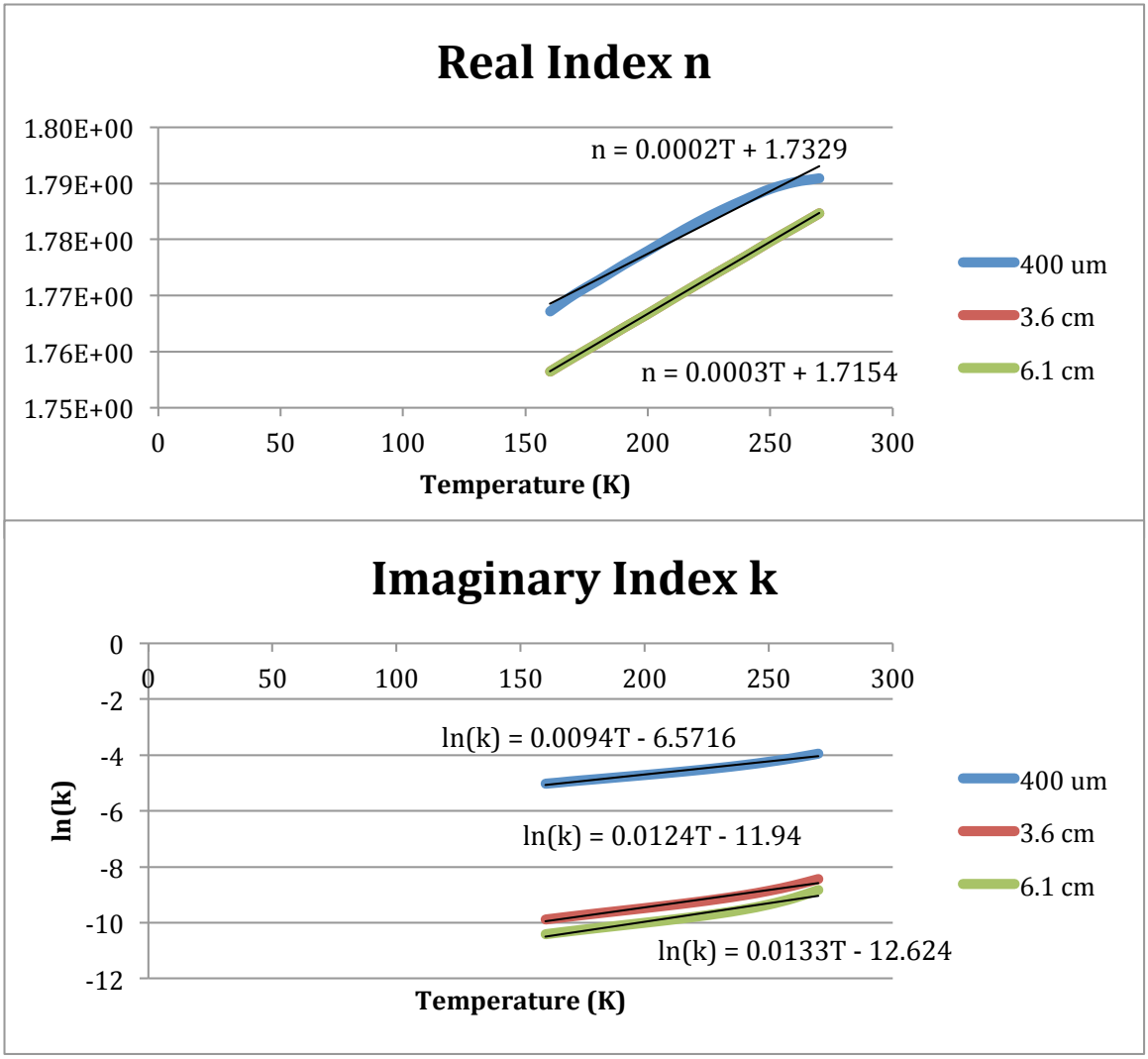

Figure 41: Data interpolation of real and imaginary components of refractive index.

7.2.1 Electric Permittivity and Magnetic Permeability:

Typically for different dielectric and paramagnetic materials, the electric and magnetic fields within the media have a different magnitude than the same fields in a vacuum. In fact, the magnitudes are proportional. These proportionality constants are defined to be the electric permittivity ϵ and magnetic permeability μ.[42] These constants are crucial to the understanding of electrodynamics, as solving Maxwell's equations shows that the speed of light is determined by the permittivity and permeability of free space where

$$c = \frac{1}{\sqrt{\epsilon_0 \mu_0}}$$

This relationship between speed and electrical constants shows us that the ratio of light speed within a vacuum to media is

$$\frac{c}{v} = \frac{1}{\sqrt{\epsilon_0 \mu_0}} \Big/ \frac{1}{\sqrt{\epsilon \mu}} = \sqrt{\frac{\epsilon \mu}{\epsilon_0 \mu_0}} = \sqrt{\epsilon_r \mu_r}$$

In the previous equation, we can define the relative permittivity ϵ_r and permeability μ_r to be the ratio of the absolute permittivity to the constants in free space. Konopinski shows that a new definition of the complex index of refraction is given by[43]

$$m^2 = (n + ik)^2 = \epsilon_r \mu_r + i\left(\frac{4\pi\gamma\mu}{\omega}\right)$$

In the previous equation, γ is the specific conductivity of the material,[44] and ω is angular velocity $\omega = \frac{2\pi c}{\lambda}$. With this definition, we have the relationships to convert between indices of refraction and electrical constants:

$$n^2 - k^2 = \epsilon_r \mu_r$$

$$2nk = \frac{4\pi\gamma\mu}{\omega}$$

For the purposes of Saturn, we will assume that the ice particles in Saturn's rings are not significantly magnetic, and that the relative magnetic permeability is thus

$$\mu_r \approx 1$$

[42] Griffiths, D. 1999. Introduction to Electrodynamics. Upper Saddle River, NJ: Prentice-Hall. 180.
[43] Konopinski, E. 1981. Electromagnetic Fields and Relativistic Particles. New York, NY: McGraw-Hill, Inc. 583.
[44] Konopinski, 580.

7.3 Monochromatic Luminosity:

As astronomy is a primarily observational science, astronomers try to understand the relationship between intrinsic properties of objects with the observed measurements. Thus by looking at the light coming from stars, planets, or galaxies, we can relate the intrinsic luminosity (energy emitted per second) to the radiant flux observed (power per unit area). Because the intensity of light falls off by $1/\,d^2$ for a distance d away from earth, then

$$L_\lambda = 4\pi d^2 F_\lambda$$

By looking at one specific wavelength λ, this is the definition of monochromatic luminosity.[45]

7.3.1 Efficiency Factors:

Depending on the size of the ring particles and the wavelength considered, the analysis of luminosity and polarization must be treated differently. For a quantitative comparison, we can define a parameter

$$x = \frac{2\pi a}{\lambda}$$

With this definition, parameter x decreases in value when the particle size a decreases, or when the wavelength of light λ increases. In the situation when the absolute value of the product of x and the complex index of refraction is less than unity, $|mx| \ll 1$, we must use the efficiency factors.

The absorption efficiency is defined as

$$Q_A = -4x\, Im\left(\frac{m^2-1}{m^2+2}\right)$$

The scattering efficiency is defined as [46]

$$Q_S = \frac{8}{3}x^4\left|\frac{m^2-1}{m^2+2}\right|^2$$

[45] Carroll, B., Ostlie, D. 2007. *An Introduction to Modern Astrophysics, 2nd ed.* San Francisco, CA: Addison-Wesley. 75.

[46] Spitzer, L. 1998. *Physical Processes in the Interstellar Medium.* New York, NY: John Wiley & Sons, Inc. 151.

7.3.2 Blackbody Radiation:

Blackbody radiation is the temperature dependent distribution of emitted electromagnetic radiation of an ideal emitter. This emitter is called a blackbody. Consider a box that acts like a blackbody at a given temperature. We know that the radiation that exists within the box must have wavelength proportional to the length of the box. These are the standing wave modes of various wavelengths. Classical theory hypothesized that the box should possess an infinite number of modes, leading to an infinite number of waves giving an infinite amount of energy. Not physically possible, this scenario describes what was called the "ultraviolet catastrophe." When incorporating quantum mechanics, it was seen that the proportion of waves at lower wavelength was much lower than other wavelengths, solving this catastrophe.[47]

Most opaque bodies are approximately blackbodies in some form. For humans, our body temperature leads to a peak in infrared emission, which is how heat vision is effective. For ice particles at 70 K, they emit primarily at submillimeter wavelengths. Max Planck derived the brightness of a blackbody (in $\frac{Watts}{m^2}\frac{1}{m}\frac{1}{steradian}$) as

$$B_\lambda(T) = \left(\frac{2hc^2}{\lambda^5}\right)\frac{1}{e^{\frac{hc}{\lambda k_B T}} - 1}$$

This helps us estimate the monochromatic luminosity, because the monochromatic flux on the surface of a blackbody is[48]

$$F_\lambda \equiv \int_{source} B_\lambda(T)\cos\theta_1\, d\Omega$$

Where $\theta_1$is the angle between the normal vector of the detector and the source. For our purposes, Saturn is so far away that $\cos\theta_1 \approx 1$. With this approximation, we can attain the monochromatic luminosity of a blackbody of radius "a" by integrating the flux over the surface area of the particle and over the solid angle $d\Omega = \sin\theta\, d\theta d\phi$ over all space.

$$L_\lambda = \int F_\lambda dA = \int\int B_\lambda(T) dA d\Omega = 4\pi^2 a^2 B_\lambda(T)$$

[47] Schroeder, D. 2000. An Introduction to Thermal Physics. San Francisco, CA: Addison Wesley Longman. 288.

[48] Léna, P., Lebrun, F., Mignard, F. 1998. *Observational Astrophysics*. Berlin, Germany: Springer-Verlag Berlin Heidelberg. 81.

If a body is not a perfect emitter, the monochromatic luminosity must be adjusted. Also Kirchoff's laws tell us that coefficients of emissivity and absorptivity are equal in magnitude.[49] Thus in the limit where $|mx| \ll 1$, the adjusted monochromatic luminosity from Table 7.1 is defined as:

$$L_\lambda = Q_A 4\pi^2 a^2 B_\lambda(T)$$

7.3.3 Reflection Luminosity:

To estimate the amount of luminosity reflected by the particles, we assume the radiation reflected stems from Saturn as a blackbody emitter. Thus

$$L_\lambda = \pi a^2 F_\lambda(Saturn)$$

We assume that approximately 100% of the light received is reflected by a particle of effective cross-sectional area $A = \pi a^2$. Also implicit in this calculation is that the ring particles are exposed to complete illumination of Saturn—the particles do not shadow each other. In our order of magnitude estimation of particle distribution, this approximation is sufficient.

Also implicit in this calculation is that the reflection is isotropic, equal in magnitude in every direction. This is not physically true, but for an order of magnitude estimate, this approximation is also sufficient.

Thus the monochromatic flux received from Saturn is

$$F_\lambda(Saturn) = \int_{Saturn} B_\lambda(T) d\Omega = B_\lambda(81.1\ K)\Omega$$

Provided by NASA's Saturn fact sheet, the blackbody temperature of Saturn is 81.1 K.[50]

In this case, the solid angle is the angle subtended by Saturn from the perspective of a B-ring particle. Because the B-ring ranges from $R = 1.52R_S$— $1.95R_S$, I estimated an average B-ring particle to be at $R \approx 1.735R_S$.[51]

[49] Spitzer, 34.

[50] Williams, D. 2010. "Saturn Fact Sheet". NASA, 17 Nov. 2010. Web. 8 May 2013. <http://nssdc.gsfc.nasa.gov/planetary/factsheet/saturnfact.html>.

[51] Filacchione, G., Capaccioni, F., et al. 2013. The Radial Distribution of Water Ice and Chromophores Across Saturn's System. *The Astrophysical Journal* 766: 776-771. 777.

Using geometrical arguments by defining the spherical coordinate system given by Figure 41, we can see that the planet of Saturn only subtends an angle of $2\theta = 2\tan^{-1}\left(\frac{1}{1.735}\right) = 1.046\,radians$. Thus the solid angle is

$$\Omega = \int_0^{0.523} \sin\theta\, d\theta \int_0^{2\pi} d\phi = 0.839471$$

Thus the reflected luminosity is given by

$$L_\lambda = \pi a^2 (0.838471) B_\lambda (81.1K)$$

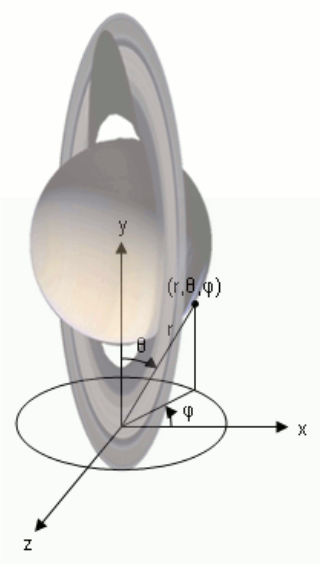

Figure 42: Coordinate axis definition for solid angle calculation.

7.3.4 Scattering Luminosity:

Besides reflecting incident radiation, the particles may also scatter light. Again the effective cross sectional area is $A = \pi a^2$. We are assuming scattering is isotropic, which is a much better approximation for Rayleigh scattering. The mechanism of Rayleigh scattering exhibits nearly equal scattering in all directions. The monochromatic flux of Saturn is the same as previously defined. In the limit that $|mx| \ll 1$, we must use the scattering efficiency such that

$$L_\lambda = Q_S \pi a^2 F_\lambda (Saturn)$$

Thus when the particle is bigger than the incident wavelength, we use reflection luminosity. While if particles are smaller than the incident wavelength, we use the scattering luminosity.

7.4 Polarization Mechanisms:

With the three types of luminosity discussed (blackbody, reflected, and scattered), we must now determine how much of each radiation is polarized. In the next sections, we will discuss how to determine P, the fraction of light polarized. We can then calculate the polarized flux by the equation

$$PF(\lambda) = \frac{1}{4\pi d^2} P L_\lambda$$

In this equation, "d" is the distance from Earth to Saturn. The polarization P is always a number between zero and unity. We will assume that reflection and scattering may induce polarization, but blackbody emission is unpolarized. There is no geometrical argument why blackbody emission should preferentially choose one orientation in which to polarize light.

7.4.1 Reflection Polarization:

The degree of polarization depends on the angle of incidence defined in the figure. As Konopinski mentions, we can define the effective complex index of refraction by

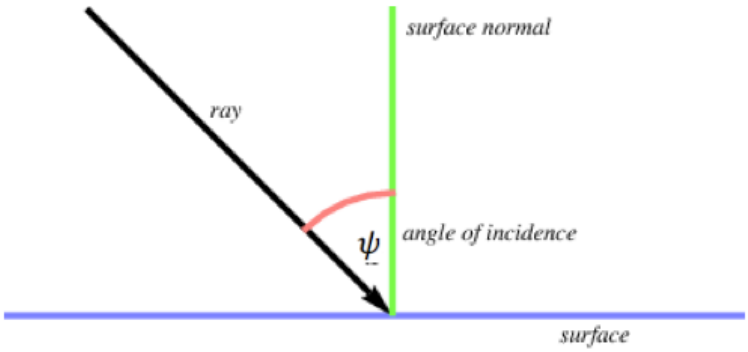

Figure 43: Definition of angle of incidence.

$$m(\psi) = n(\psi) + ik(\psi) \equiv \sqrt{m^2(0) - \sin^2\psi}$$

In this notation, $m(0) = n(0) + ik(0)$ where $m(0), n(0), k(0)$ are all the original indices defined by section 7.2.[52]

The polarization by reflection is defined to be[53]

$$P_{reflect} = \left|\frac{R_\parallel - R_\perp}{R_\parallel + R_\perp}\right|$$

The coefficients of parallel and perpendicular reflection that are needed for the polarization calculation are derived from the Fresnel equations by Konopinski as[54]

$$R_\parallel = \frac{[\mu_r \cos\psi - n(\psi)]^2 + k(\psi)^2}{[\mu_r \cos\psi + n(\psi)]^2 + k(\psi)^2}$$

$$R_\perp = \frac{[\epsilon_r \cos\psi - n(\psi)]^2 + \left[\left(\frac{4\pi\gamma}{\omega}\right)\cos\psi - k(\psi)\right]^2}{[\epsilon_r \cos\psi + n(\psi)]^2 + \left[\left(\frac{4\pi\gamma}{\omega}\right)\cos\psi + k(\psi)\right]^2} = \frac{[3\cos\psi - n(\psi)]^2 + [2n(0)k(0)\cos\psi - k(\psi)]^2}{[3\cos\psi + n(\psi)]^2 + [2n(0)k(0)\cos\psi + k(\psi)]^2}$$

We chose to use the notation of indices rather than conductivity. Also by Iwabuchi et al., we can approximate the relative permittivity by[55]

$$\epsilon_r = 3.1884 + 0.00091(T - 273) \approx 3.00$$

We assume an angle of incidence of $\psi = \frac{\pi}{4}$, because that is the most likely angle from the ansae due to the position of the particles with respect to Saturn.

[52] Konopinski, 587.
[53] Born M., Wolf E. 1999. Principles of Optics. Cambridge: Cambridge University Press. 46.
[54] Konopinski, 589.
[55] Iwabuchi, 2521.

7.4.2 Scattering Polarization:

As depicted from Figure 4 in section 1.2, the amount of polarization observed from scattered light is dependent on the angle of observation, θ. At $\theta = 0$ (forward scattering) and $\theta = \pi$ (back scattering), we observe no polarization. However at an angle of $\theta = \frac{\pi}{2}$, we expect the light to be 100% polarized in the +Q orientation—vertically polarized light.

This phenomenon can be quantified by[56]

$$P_{scatter} = \frac{\sin^2\theta}{1 + \cos^2\theta}$$

Saying the scattering is at $\theta = \frac{\pi}{2}$ is ideal, but most likely inaccurate. We assume a scattering angle of $\theta = 80°$, as the ring is inclined by an order of $10°$. This leads to a polarization of

$$P_{scatter} = \frac{\sin^2 80°}{1 + \cos^2 80°} \approx 0.941$$

Scattering should result in approximately 94.1% polarization of the scattering luminosity.

7.5 Total Polarization:

We can now define the total polarized flux to be the sum of polarized flux from each mechanism and for each particle. If we include the number of boulders, pebbles, large grains, and small grains $N_B, N_P, N_L,$ and N_S, then the total polarized flux is

$$PF(\lambda) = \frac{1}{4\pi d^2}\left[\sum_{j=B,P,L,and\ S} N_j\left(P_{S/R}L_{S/R}\right)\right]$$

Here, the S/R notation means whichever scattering or reflection mechanism is used for that particular particle. This is determined by the size of the particle and wavelength, but the mechanisms are already tabulated in Table 7.1. Similarly, the total flux is the sum of the scattering/reflection luminosity with the blackbody emission luminosity. Again the type of blackbody radiation for each particle is noted in section 7.1.

$$TF(\lambda) = \frac{1}{4\pi d^2}\left[\sum_{j=B,P,L,and\ S} N_j\left(L_{S/R}\right) + \sum_{j=B,P,and\ D} N_j(L_E)\right]$$

We can define the total polarization per wavelength as a fraction of polarized to total flux:

$$P(\lambda) = \frac{PF(\lambda)}{TF(\lambda)}$$

[56] Born and Wolf, 783.

7.6 Constraining Particle Counts:

After tabulating the different polarized fluxes, we can now determine the number of particles in our model that would reproduce the data observed at 0.4 mm, 3.6 cm, and 6.1 cm. In our analysis, we are determining the number of particles per 10 m boulder. To do this, we set $N_B = 1$.

To determine the other numbers, we utilize the power law distribution provided by French and Nicholson:[57]

$$N(a)da = C_0 a^{-q} da$$

The parameters in this equation are the number of particles of radius "a" $N(a)$ and some constants C_0 and q. French and Nicholson mention that this law is only accurate for the range of particle size "a" between $a_{\min} = 30\,cm$ and $a_{\max} = 20\,m$. However, Esposito mentions that $a_{\min}$ can range to as low as $a_{\min} = 1\,cm$.[58]

For the B-ring of Saturn, French and Nicholson estimate a constant of $q = 2.75$. Thus to find the number of particles per boulder, we can divide power laws to see

$$\frac{N_j}{N_B} = \frac{a_j^{-q}}{a_B^{-q}} = \frac{(d_j)^{-q}}{10^{-q}}$$

7.6.1 Number of Pebbles:

To find the number of pebbles of size $d = 2a_P = 0.01\,m$, we can simply use the power law provided above. This gives us a hard estimate that we can set fixed in the rest of our analysis.

$$\frac{N_P}{N_B} = \frac{a_P^{-q}}{a_B^{-q}} \approx 1.77{\times}10^8\ pebbles\ per\ boulder$$

By just adding these two parameters $N_B = 1$ and $N_P = 1.77{\times}10^8$, and setting the other two parameters to zero, we attain the polarizations

$$P(0.4mm) = 0.0569 = 5.69\%$$
$$P(3.6cm) = 0.728 = 72.8\%$$
$$P(6.1cm) = 0.298 = 29.8\%$$

[57] French, R., Nicholson, P. 2000. Saturn's Rings II: Particle Sizes Inferred from Stellar Occultation Data. *Icarus* 145: 502-523. 505.
[58] Esposito, 386.

What this shows is that our very crude toy model can account for the polarization seen at radio wavelengths within about a factor of two, which gives some support to our model. However, our model does not account for the polarization seen at $0.4\ mm$. This polarization of 5.69% is dominated by the reflection component of pebble-sized particles. Thus we may be overestimating the reflection contribution. In fact, for the remainder of this paper, we will assume that this is the case. We will assume our reflection model is inaccurate, but the scattering model is approximately correct. Thus we will look for increases in polarization greater than $P_{5\sigma} = 0.530\%$ above $P(0.4mm) = 5.69\%$ (i.e. $P(0.4\ mm) \geq 6.22\%$). We assert that SHARP would have easily detected these fluctuations due to scattering if the polarization were that significant, so they must not be present.

7.6.2 Number of Large Grains:

Trying to determine the number of large grains is not as easy as for pebbles. The size of dust grains does not lie in the range of acceptable values for the power law. However, if we were to temporarily assume that the power law extends to sizes of large grains $d = 2a_L = 1{\times}10^{-4}\ m$, we would infer the number of large dust grains per boulder as

$$\frac{N_L}{N_B} = \frac{a_L^{-q}}{a_B^{-q}} \approx 5.62{\times}10^{13}\ large\ grains\ per\ boulder$$

However, using this parameter with the N_B and N_P above gives the polarizations

$$P(0.4mm) = 0.286 = 28.6\%$$
$$P(3.6cm) = 0.728 = 72.8\%$$
$$P(6.1cm) = 0.298 = 29.8\%$$

While the radio polarizations did not change at all, the submillimeter polarization spiked by a factor of 4. SHARP would have easily detected a polarization that large. Thus, if our toy model for scattering is correct, we can conclusively rule out the power law provided by French and Nicholson extending only to large grains as a minimum radius.

7.6.3 Number of Small Grains:

We have shown that we can rule out the power law extending down only to large grains. The addition of even smaller dust grains is interesting. For small dust grains $d = 2a_S = 1\times10^{-5}\,m$, their blackbody luminosity is larger in magnitude than scattering luminosity for 0.4 mm. This means that for small grains (unlike every other particle size), adding more particles actually decreases the polarization at 0.4 mm. Theoretically, we could cancel out the $P(0.4\,mm) = 26.1\%$ measurement above by adding $N_D = 1\times10^{20}$ dust grains. However, we argue that this is unlikely, as an N_S that large implies that most of the mass in Saturn's rings is comprised of dust particles. A result that significant would have probably been detected before.

For sake of experiment, if we use the previously defined parameters for the number of particles and use the power law for small grains, we obtain

$$\frac{N_S}{N_B} = \frac{a_S^{-q}}{a_B^{-q}} \approx 3.16\times10^{16}\ dust\ grains\ per\ boulder$$

By using this number obtained by extending the power law even further to small dust grains, we obtain polarizations of

$$P(0.4mm) = 0.286 = 27.5\%$$
$$P(3.6cm) = 0.728 = 72.8\%$$
$$P(6.1cm) = 0.298 = 29.8\%$$

Similar to the arguments in this section, we can conclude that the power law cannot be extended down to small grains as well, assuming our model for scattering is correct. SHARP would have been able to detect a 27.5% polarization at 0.4 mm.

We can summarize these results by Table 7.6 below. For these calculations, $N_B = 1$ and $N_P = 1.77\times10^8$, while both N_L and N_S can vary to show varying submillimeter 0.4 mm polarization.

N_L	0	5.62×10^{13}	5.62×10^{13}
N_S	0	0	3.16×10^{16}
$P(3.6\ cm)$	5.69%	28.6%	27.5%
$P(6.1\ cm)$	72.8%	72.8%	72.8%
$P(0.4mm)$	29.8%	29.8%	29.8%

Table 7.6: Change of Polarization as a function of large grain number and small grain number.

7.7 Results and Implications:

Our toy model that comprised of boulders, pebbles, large grains, and dust grains proved to be adequately successful in explaining the polarizations at radio wavelengths that Van der Tak et al. had observed using the VLA. However, the polarization that SHARP sees at submillimeter wavelengths was not reproduced accurately, as we assume our model's polarization by reflection is too large at submillimeter wavelengths. We were able to estimate the number of pebbles by using the power law provided by French and Nicholson, however there exists a disagreement in the minimum radius $a_{\min}$ for which the power law is valid. Assuming our toy model's scattering is approximately correct, we can conclude that the power law is invalid when extending the minimum radius to large dust grains of $a_{\min} = 1 \times 10^{-4}\ m$ or small dust grains of $a_{\min} = 1 \times 10^{-5}\ m$.

However, because of the fact that increasing the number of small dust particles decreases the submillimeter polarization, we are unable with this model to set an upper limit constraint to either the number of large dust grains or the number of small dust grains. We are, however, able to conclude that the power law cannot approximate these numbers.

A key fact that we have shown in this project is the sensitivity of 0.4 mm polarization to dust. By varying large grains and dust grains, the polarization at 0.4 mm fluctuated significantly, leaving the radio polarizations relatively unchanged. This sensitivity shows the utility of SHARP and other submillimeter polarimetry projects in constraining particle sizes smaller than millimeter diameter.

Overall, we established a 5σ upper limit of $P_{5\sigma} < 0.530\%$ for polarization in Saturn's B ring at 350 μm and 450 μm. Our toy model describes the polarization by Rayleigh scattering produced from radio wavelengths observed by Van der Tak et al., but it fails to model the correct reflected polarization. Trying to constrain the number of particles with our scattering model, we were able to utilize the power law distribution to attain size distributions for pebbles per boulder, but we were unable to constrain the number of large dust grains and small dust grains due to the decreased polarization by small grains. We have concluded that the power law does not accurately represent the particle size distribution for sizes smaller than 1 cm.

7.8 Future Work:

As a very crude toy model for the particles in Saturn's rings, we are very satisfied to find our model reproduces the results of Van der Tak et al. within a factor of two. However, this project did make many approximations, and the result could be improved with more precision.

As a few suggestions, the absorbance within the index of refraction could be estimated more accurately. The imaginary index is most likely too low, as the reddish color of Saturn's rings implies a higher absorption coefficient.[59]

We could also consider more particle sizes, as different sizes apparently have opposing effects. Having a representative particle for each magnitude of size may change the result.

As more data arises, polarizations at different wavelengths offer more details on particle distribution. Longer and shorter wavelengths could give crucial evidence toward particle constraints.

The angles for reflection and scattering could be estimated with more accuracy by considering the exact three-dimensional geometry of Saturn to its rings and Earth. The approximations were sufficient for our order of magnitude calculations, but more precise calculations may show the reflection contributing too much in our model.

By a more exhaustive literature survey, other constraints of $a_{\min}$ could be considered by looking into fields other than polarimetry.

There is plenty of room for improvement, but this project shows the potential for future work in submillimeter polarimetry and its determination of particle sizes.

[59] Esposito, 387.

References

Attard, M., Houde, M., Novak, G., et al. 2009. Magnetic Fields and Infall Motions In NGC 1333 IRAS 4. *The Astrophysical Journal* 702: 1584-1592.

Bevington, P., Robinson, D. 2002. *Data Reduction and Error Analysis for the Physical Sciences*. New York, NY: McGraw-Hill, Inc.

Born M., Wolf E. 1999. *Principles of Optics*. Cambridge: Cambridge University Press.

Carroll, B., Ostlie, D. 2007. *An Introduction to Modern Astrophysics, 2nd ed.* San Francisco, CA: Addison-Wesley.

Esposito, L.W. 2010. Composition, Structure, Dynamics, and Evolution of Saturn's Rings. *Annual Review of Earth and Planetary Sciences* 38:383-410.

Ferrari, C., Reffet, E. 2013. The Dark Side of Saturn's B Ring: Seasons as Clues to its Structure. *Icarus* 223: 28-39.

Filacchione, G., Capaccioni, F., et al. 2013. The Radial Distribution of Water Ice and Chromophores Across Saturn's System. *The Astrophysical Journal* 766: 766-771.

French, R., Nicholson, P. 2000. Saturn's Rings II: Particle Sizes Inferred from Stellar Occultation Data. *Icarus* 145: 502-523.

Griffiths, D. 1999. *Introduction to Electrodynamics.* Upper Saddle River, NJ: Prentice-Hall.

Hecht, E. 1998. *Optics*. Reading, MA: Addison Wesley Longman, Inc.

Hedman, M.M., et al. 2011. The Christiansen Effect in Saturn's Narrow Dusty Rings and the Spectral Identification of Clumps in the F Ring. *Icarus* 215:695-711.

Hildebrand, R.H., Davidson, J.A., et al. 2000. A Primer on Far-Infrared Polarimetry. *Publications of the Astronomical Society of the Pacific* 112: 1215-1235.

"HORIZONS Web-Interface." Jet Propulsion Laboratory – California Institute of Technology. Web. 8 May 2013. <http://ssd.jpl.nasa.gov/horizons.cgi>.

Iwabuchi, H., Yang, P. 2011. Temperature Dependence of Ice Optical Constants: Implications for Simulating the Single-Scattering Properties of Cold Ice Clouds. *Journal of Quantitative Spectroscopy & Radiative Transfer* 112: 2520-2525.

Kantelberg, R. 2013. "Ring-Plane Crossing." Astro-Imaging, 30 Mar. 2013. Web. 8 May 8, 2013.<http://www.astroimaging.com/Gallery/Solarsystem/Saturn/Ringplane/Ring_plane.html>.

"Key Concepts of the Electromagnetic Wave." Journal of Informational Medicine. Web. 8 May 2013. < http://journalinformationalmedicine.org/keycon.htm>.

Konopinski, E. 1981. *Electromagnetic Fields and Relativistic Particles*. New York, NY: McGraw-Hill, Inc.

Krejny, M. 2008. The Hertz-VPM Polarimeter and Applications of Multiwavelength Polarimetry. Ph.D dissertation, Northwestern University.

Krejny, M., Matthews T., Novak, G., Cho, J., Li, H., Shinnaga, H., Vaillancourt, J.E. 2009. Polarimetry of DG Tau at 350 μm. *The Astrophysical Journal* 705:717-722.

Léna, P., Lebrun, F., Mignard, F. 1998. *Observational Astrophysics*. Berlin, Germany: Springer-Verlag Berlin Heidelberg.

Li, H., Dowell, C.D., Kirby, L., Novak, G., Vaillancourt, J.E. 2008. Design and Initial Performance of SHARP, a Polarimeter for the SHARC-II Camera at the Caltech Submillimeter Observatory. *Applied Optics 47: 422-430.*

Meyer-Arendt J.R. 1995. *Introduction to Classical and Modern Optics*. Englewood Cliffs, NJ: Prentice Hall.

"Pink Noise Spectrum." Wikimedia Commons. Web. 8 May 2013. <https://commons.wikimedia.org/wiki/File:Pink_noise_spectrum.png>.

Schmidt J, et al. 2009. Dynamics of Saturn's dense rings. See Dougherty et al. 2009, pp. 413–58.

Schroeder, D. 2000. *An Introduction to Thermal Physics*. San Francisco, CA: Addison Wesley Longman.

Spitzer, L. 1998. *Physical Processes in the Interstellar Medium.* New York, NY: John Wiley & Sons, Inc.

Vahidinia S., et al. 2011. Saturn's F Ring Grains: Aggregates are Made of Crystalline Water Ice. *Icarus* 215: 682-694.

Van de Hulst, H.C. 1957. *Light Scattering by Small Particles*. New York, John Wiley & Sons Inc.

Van der Tak F., Pater, I., Silva, A., Millan, R. 1999. Time Variability in the Radio Brightness Distribution of Saturn. *Icarus* 142:125-147.

Watanabe, S. 2008. "Saturn's Rings, Cold and Colder." NASA, 29 Apr. 2008. Web. 8 May 2013. < http://www.nasa.gov/mission_pages/cassini/multimedia/pia06425.html>.

Williams, D. 2010. “Saturn Fact Sheet”. NASA, 17 Nov. 2010. Web. 8 May 2013. <http://nssdc.gsfc.nasa.gov/planetary/factsheet/saturnfact.html>.

“Wire-Grid Polarizer.” Wikimedia Commons. Web. 8 May 2013. <https://commons.wikimedia.org/wiki/File:Wire-grid-polarizer.svg>.

Appendix A: Table of Saturn Data

April 2007:

File number	File Type	Date	Wavelength	Tau (at 1.3mm)	Zenith Angle	Transmission (e^-25tsecz)	Distance to Earth (Light minutes)	Distance to Earth (AU)	North Pole Position Angle	Ring Plane Inclination
38329	dither (4 files)	4/29/07	350	0.064	42	0.116133793	74.667466	8.977960281	353.4356	-15.4
38330	dither (4 files)	4/29/07	350	0.064	42	0.116133793	74.667466	8.977960281	353.4356	-15.4
38331	dither (4 files)	4/29/07	350	0.064	42	0.116133793	74.667466	8.977960281	353.4356	-15.4
38332	dither (4 files)	4/29/07	350	0.064	42	0.116133793	74.667466	8.977960281	353.4356	-15.4
38333	dither (4 files)	4/29/07	350	0.048	49	0.16055741	74.667466	8.977960281	353.4356	-15.4
38334	dither (4 files)	4/29/07	350	0.048	49	0.16055741	74.667466	8.977960281	353.4356	-15.4
38335	dither (4 files)	4/29/07	350	0.048	49	0.16055741	74.667466	8.977960281	353.4356	-15.4
38336	dither (4 files)	4/29/07	350	0.048	49	0.16055741	74.667466	8.977960281	353.4356	-15.4
38444	dither (4 files)	5/1/07	350	0.068	42	0.101512266	74.940741	9.010818663	353.4368	-15.4
38445	dither (4 files)	5/1/07	350	0.068	42	0.101512266	74.940741	9.010818663	353.4368	-15.4
38446	dither (4 files)	5/1/07	350	0.068	42	0.101512266	74.940741	9.010818663	353.4368	-15.4
38447	dither (4 files)	5/1/07	350	0.068	42	0.101512266	74.940741	9.010818663	353.4368	-15.4
38448	dither (4 files)	5/1/07	350	0.066		0.192049909	74.940741	9.010818663	353.4368	-15.4
38449	dither (4 files)	5/1/07	350	0.066		0.192049909	74.940741	9.010818663	353.4368	-15.4
38450	dither (4 files)	5/1/07	350	0.066		0.192049909	74.940741	9.010818663	353.4368	-15.4
38451	dither (4 files)	5/1/07	350	0.066		0.192049909	74.940741	9.010818663	353.4368	-15.4

May 2008:

File number	File Type	Date	Wavelength	Tau (at 1.3mm)	Zenith Angle	Transmission (e^-25tsecz)	Distance to Earth (Light minutes)	Distance to Earth (AU)	North Pole Position Angle	Ring Plane Inclination
43292	dither (4 files)	5/9/08	350	0.017	16	0.642667844	75.034897	9.02213991	354.0154	-7
43293	dither (4 files)	5/9/08	350	0.017	16	0.642667844	75.034897	9.02213991	354.0154	-7
43294	dither (4 files)	5/9/08	350	0.039	18	0.358733442	75.034897	9.02213991	354.0154	-7
43295	dither (4 files)	5/9/08	350	0.039	18	0.358733442	75.034897	9.02213991	354.0154	-7
43296	dither (4 files)	5/9/08	350	0.039	18	0.358733442	75.034897	9.02213991	354.0154	-7
43297	dither (4 files)	5/9/08	350	0.039	18	0.358733442	75.034897	9.02213991	354.0154	-7
43298	dither (4 files)	5/9/08	350	0.062	25	0.180823154	75.034897	9.02213991	354.0154	-7
43299	dither (4 files)	5/9/08	350	0.062	25	0.180823154	75.034897	9.02213991	354.0154	-7
43300	dither (4 files)	5/9/08	350	0.062	25	0.180823154	75.034897	9.02213991	354.0154	-7
43301	dither (4 files)	5/9/08	350	0.062	25	0.180823154	75.034897	9.02213991	354.0154	-7
43302	dither (4 files)	5/9/08	350	0.04	31	0.311413584	75.034897	9.02213991	354.0154	-7
43303	dither (4 files)	5/9/08	350	0.04	31	0.311413584	75.034897	9.02213991	354.0154	-7
43304	dither (4 files)	5/9/08	350	0.04	31	0.311413584	75.034897	9.02213991	354.0154	-7
43305	dither (4 files)	5/9/08	350	0.04	31	0.311413584	75.034897	9.02213991	354.0154	-7
43306	dither (4 files)	5/9/08	350	0.032	38	0.362324677	75.034897	9.02213991	354.0154	-7
43307	dither (4 files)	5/9/08	350	0.032	38	0.362324677	75.034897	9.02213991	354.0154	-7
43308	dither (4 files)	5/9/08	350	0.032	38	0.362324677	75.034897	9.02213991	354.0154	-7
43309	dither (4 files)	5/9/08	350	0.032	38	0.362324677	75.034897	9.02213991	354.0154	-7
43311	dither (4 files)	5/9/08	350	0.008	47	0.745831305	75.034897	9.02213991	354.0154	-7
43312	dither (4 files)	5/9/08	350	0.008	47	0.745831305	75.034897	9.02213991	354.0154	-7
43313	dither (4 files)	5/9/08	350	0.008	47	0.745831305	75.034897	9.02213991	354.0154	-7
43314	dither (4 files)	5/9/08	350	0.008	47	0.745831305	75.034897	9.02213991	354.0154	-7
43315	dither (4 files)	5/9/08	350	0.04	53	0.189827381	75.034897	9.02213991	354.0154	-7
43316	dither (4 files)	5/9/08	350	0.04	53	0.189827381	75.034897	9.02213991	354.0154	-7
43317	dither (4 files)	5/9/08	350	0.04	53	0.189827381	75.034897	9.02213991	354.0154	-7
43318	dither (4 files)	5/9/08	350	0.04	53	0.189827381	75.034897	9.02213991	354.0154	-7
43319	dither (4 files)	5/9/08	350	0.041	63	0.104584858	75.034897	9.02213991	354.0154	-7
43320	dither (4 files)	5/9/08	350	0.041	63	0.104584858	75.034897	9.02213991	354.0154	-7
43321	dither (4 files)	5/9/08	350	0.041	63	0.104584858	75.034897	9.02213991	354.0154	-7
43322	dither (4 files)	5/9/08	350	0.041	63	0.104584858	75.034897	9.02213991	354.0154	-7
43323	dither (4 files)	5/9/08	350	0.034	68	0.103410674	75.034897	9.02213991	354.0154	-7
43324	dither (4 files)	5/9/08	350	0.034	68	0.103410674	75.034897	9.02213991	354.0154	-7
43325	dither (4 files)	5/9/08	350	0.034	68	0.103410674	75.034897	9.02213991	354.0154	-7
43326	dither (4 files)	5/9/08	350	0.034	68	0.103410674	75.034897	9.02213991	354.0154	-7

January 2009:

File number	File Type	Date	Wavelength	Tau (at 1.3mm)	Zenith Angle	Transmission (e^-25tsecz)	Distance to Earth (Light minutes)	Distance to Earth (AU)	North Pole Position Angle	Ring Plane Inclination
46207	dither (4 files)	1/25/09	350	0.027	47	0.37167389	72.063179	8.664822759	355.2161	-1.2
46208	dither (4 files)	1/25/09	350	0.027	47	0.37167389	72.063179	8.664822759	355.2161	-1.2
46209	dither (4 files)	1/25/09	350	0.027	47	0.37167389	72.063179	8.664822759	355.2161	-1.2
46210	dither (4 files)	1/25/09	350	0.027	47	0.37167389	72.063179	8.664822759	355.2161	-1.2

May 2010:

File number	File Type	Date	Wavelength	Tau (at 1.3mm)	Zenith Angle	Transmission (e^-25tsecz)	Distance to Earth (Light minutes)	Distance to Earth (AU)	North Pole Position Angle	Ring Plane Inclination
50242	dither (3 files)	4/22/10	350	0.039	40	0.280054204	72.193192	8.680455425	354.8271	2.4
50242	dither (3 files)	4/22/10	350	0.039	40	0.280054204	72.193192	8.680455425	354.8271	2.4
50242	dither (3 files)	4/22/10	350	0.039	40	0.280054204	72.193192	8.680455425	354.8271	2.4
50245	dither (1 file)	4/22/10	350			1	72.193192	8.680455425	354.8271	2.4
50254	dither (4 files)	4/22/10	350	0.044	24	0.299961872	72.193192	8.680455425	354.8271	2.4
50255	dither (4 files)	4/22/10	350	0.044	24	0.299961872	72.193192	8.680455425	354.8271	2.4
50256	dither (4 files)	4/22/10	350	0.044	24	0.299961872	72.193192	8.680455425	354.8271	2.4
50257	dither (4 files)	4/22/10	350	0.044	24	0.299961872	72.193192	8.680455425	354.8271	2.4
50258	dither (4 files)	4/22/10	350	0.043	19	0.320798451	72.193192	8.680455425	354.8271	2.4
50258	dither (4 files)	4/22/10	350	0.043	19	0.320798451	72.193192	8.680455425	354.8271	2.4
50258	dither (4 files)	4/22/10	350	0.043	19	0.320798451	72.193192	8.680455425	354.8271	2.4
50258	dither (4 files)	4/22/10	350	0.043	19	0.320798451	72.193192	8.680455425	354.8271	2.4
50267	dither (4 files)	4/22/10	350	0.051	18	0.261684857	72.193192	8.680455425	354.8271	2.4
50268	dither (4 files)	4/22/10	350	0.051	18	0.261684857	72.193192	8.680455425	354.8271	2.4
50269	dither (4 files)	4/22/10	350	0.051	18	0.261684857	72.193192	8.680455425	354.8271	2.4
50270	dither (4 files)	4/22/10	350	0.051	18	0.261684857	72.193192	8.680455425	354.8271	2.4
50271	dither (4 files)	4/22/10	350			1	72.193192	8.680455425	354.8271	2.4
50272	dither (4 files)	4/22/10	350			1	72.193192	8.680455425	354.8271	2.4
50273	dither (4 files)	4/22/10	350			1	72.193192	8.680455425	354.8271	2.4
50274	dither (4 files)	4/22/10	350			1	72.193192	8.680455425	354.8271	2.4
50280	dither (4 files)	4/22/10	350	0.067	38	0.119360672	72.193192	8.680455425	354.8271	2.4
50281	dither (4 files)	4/22/10	350	0.067	38	0.119360672	72.193192	8.680455425	354.8271	2.4
50282	dither (4 files)	4/22/10	350	0.067	38	0.119360672	72.193192	8.680455425	354.8271	2.4
50283	dither (4 files)	4/22/10	350	0.067	38	0.119360672	72.193192	8.680455425	354.8271	2.4
50300	dither (4 files)	4/22/10	350	0.033	61	0.182373426	72.193192	8.680455425	354.8271	2.4
50301	dither (4 files)	4/22/10	350	0.033	61	0.182373426	72.193192	8.680455425	354.8271	2.4
50302	dither (4 files)	4/22/10	350	0.033	61	0.182373426	72.193192	8.680455425	354.8271	2.4
50303	dither (4 files)	4/22/10	350	0.033	61	0.182373426	72.193192	8.680455425	354.8271	2.4
50378	dither (4 files)	4/24/10	350	0.04	25	0.331748569	72.397584	8.705031367	354.8217	2.4
50379	dither (4 files)	4/24/10	350	0.04	25	0.331748569	72.397584	8.705031367	354.8217	2.4
50380	dither (4 files)	4/24/10	350	0.04	25	0.331748569	72.397584	8.705031367	354.8217	2.4
50381	dither (4 files)	4/24/10	350	0.04	25	0.331748569	72.397584	8.705031367	354.8217	2.4
50390	dither (4 files)	4/24/10	350	0.04	17	0.351448618	72.397584	8.705031367	354.8217	2.4
50391	dither (4 files)	4/24/10	350	0.04	17	0.351448618	72.397584	8.705031367	354.8217	2.4
50392	dither (4 files)	4/24/10	350	0.04	17	0.351448618	72.397584	8.705031367	354.8217	2.4
50393	dither (4 files)	4/24/10	350	0.04	17	0.351448618	72.397584	8.705031367	354.8217	2.4
50398	dither (4 files)	4/24/10	350	0.048	23	0.27154363	72.397584	8.705031367	354.8217	2.4
50399	dither (4 files)	4/24/10	350	0.048	23	0.27154363	72.397584	8.705031367	354.8217	2.4
50400	dither (4 files)	4/24/10	350	0.048	23	0.27154363	72.397584	8.705031367	354.8217	2.4
50401	dither (4 files)	4/24/10	350	0.048	23	0.27154363	72.397584	8.705031367	354.8217	2.4

Appendix B: Table of Indices of Refraction

Real part n	Temperatures (K)					
Wavelength(um)	160	170	180	190	200	210
399.941	1.76718	1.77021	1.77277	1.77547	1.77797	1.78056
36043	1.75646	1.75906	1.7616	1.76422	1.76674	1.76937
60905.4	1.75646	1.75906	1.7616	1.76422	1.76674	1.76937
	220	230	240	250	260	270
399.941	1.78302	1.78522	1.78718	1.78901	1.79024	1.79091
36043	1.77198	1.77451	1.77701	1.77965	1.78214	1.78467
60905.4	1.77198	1.77451	1.77701	1.77965	1.78214	1.78467

Imaginary part k	Temperatures (K)			
Wavelength(um)	160	170	180	190
399.941	0.00651385	0.00713773	0.00769416	0.00830948
36043	5.07584E-05	5.65705E-05	6.26699E-05	6.92034E-05
60905.4	3.00368E-05	3.34763E-05	3.70859E-05	0.000040953
	200	210	220	230
399.941	0.00896511	0.00970425	0.0105514	0.0115561
36043	7.63888E-05	8.45491E-05	9.41719E-05	0.000106014
60905.4	4.52091E-05	5.00554E-05	5.58158E-05	6.30448E-05
	240	250	260	270
399.941	0.0127986	0.0143873	0.0164681	0.0192601
36043	0.000121296	0.000142051	0.000171756	0.000216396
60905.4	7.27547E-05	8.68643E-05	0.000109048	0.000146238

Appendix C: Polarization Calculations

Luminosity

Boulders	Wavelength	abs(mx)	F_v(Sat)	B_v(70)	Q_s
1.00E+01	4.00E-04	137201.3694	1.749E+01	1.732E+01	1.674E+19
	3.60E-02	1515.294857	3.347E-07	3.440E-07	2.497E+11
	6.10E-02	894.2723752	4.065E-08	4.178E-08	3.029E+10
Pebbles	Wavelength	abs(mx)	F_v(Sat)	B_v(70)	Q_s
1.00E-02	4.00E-04	137.2013694	1.749E+01	1.732E+01	1.674E+07
	3.60E-02	1.515294857	3.347E-07	3.440E-07	2.497E-01
	6.10E-02	0.894272375	4.065E-08	4.178E-08	3.029E-02
Large Grains	Wavelength	abs(mx)	F_v(Sat)	B_v(70)	Q_s
1.00E-04	4.00E-04	1.372013694	1.749E+01	1.732E+01	1.674E-01
	3.60E-02	0.015152949	3.347E-07	3.440E-07	2.497E-09
	6.10E-02	0.008942724	4.065E-08	4.178E-08	3.029E-10
Dust	Wavelength	abs(mx)	F_v(Sat)	B_v(70)	Q_s
1.00E-05	4.00E-04	0.137201369	1.749E+01	1.732E+01	1.674E-05
	3.60E-02	0.001515295	3.347E-07	3.440E-07	2.497E-13
	6.10E-02	0.000894272	4.065E-08	4.178E-08	3.029E-14

Q_a	Blackbody	Modified Blackbody	Scattering	Reflection
3.488E+02	**1.709E+04**	5.961E+06	2.299E+22	**1.374E+03**
2.411E-02	**3.395E-04**	8.187E-06	6.564E+06	**2.629E-05**
6.495E-02	**4.124E-05**	2.678E-06	9.669E+04	**3.192E-06**

Q_a	Blackbody	Modified Blackbody	Scattering	Reflection
3.488E-01	**1.709E-02**	5.961E-03	2.299E+04	**1.374E-03**
2.411E-05	3.395E-10	**8.187E-15**	**6.564E-12**	2.629E-11
6.495E-05	4.124E-11	**2.678E-15**	**9.669E-14**	3.192E-12

Q_a	Blackbody	Modified Blackbody	Scattering	Reflection
3.488E-03	1.709E-06	**5.961E-09**	**2.299E-08**	1.374E-07
2.411E-07	3.395E-14	**8.187E-21**	**6.564E-24**	2.629E-15
6.495E-07	4.124E-15	**2.678E-21**	**9.669E-26**	3.192E-16

Q_a	Blackbody	Modified Blackbody	Scattering	Reflection
3.488E-04	1.709E-08	**5.961E-12**	**2.299E-14**	1.374E-09
2.411E-08	3.395E-16	**8.187E-24**	**6.564E-30**	2.629E-17
6.495E-08	4.124E-17	**2.678E-24**	**9.669E-32**	3.192E-18

Polarization Angle of incidence 0.785398163

Boulders	Wavelength	Polarization by Rayleigh Scattering	R parallel	R perpendicular
1.00E+01	4.00E-04	0.941457882	1.492E-01	1.985E-02
	3.60E-02	0.941457882	1.469E-01	2.086E-02
	6.10E-02	0.941457882	1.469E-01	2.086E-02

Pebbles	Wavelength	Polarization by Rayle	R parallel	R perpendicular
1.00E-02	4.00E-04	0.941457882	1.492E-01	1.985E-02
	3.60E-02	**0.941457882**	1.469E-01	2.086E-02
	6.10E-02	**0.941457882**	1.469E-01	2.086E-02

Large Grains	Wavelength	Polarization by Rayle	R parallel	R perpendicular
1.00E-04	4.00E-04	**0.941457882**	1.492E-01	1.985E-02
	3.60E-02	**0.941457882**	1.469E-01	2.086E-02
	6.10E-02	**0.941457882**	1.469E-01	2.086E-02

Dust	Wavelength	Polarization by Rayle	R parallel	R perpendicular
1.00E-05	4.00E-04	**0.941457882**	1.492E-01	1.985E-02
	3.60E-02	**0.941457882**	1.469E-01	2.086E-02
	6.10E-02	**0.941457882**	1.469E-01	2.086E-02

Polarization by Reflection	Scattering Polarized Flux	Reflection Polarized Flux	N_B
7.652E-01	2.165E+22	**1.051E+03**	**1.00E+00**
7.513E-01	6.180E+06	**1.975E-05**	
7.513E-01	9.103E+04	**2.398E-06**	

Polarization by Reflection	Scattering Polarized Flux	Reflection Polarized Flux	N_P
7.652E-01	2.165E+04	**1.051E-03**	**177000000**
7.513E-01	**6.180E-12**	1.975E-11	
7.513E-01	**9.103E-14**	2.398E-12	

Polarization by Reflection	Scattering Polarized Flux	Reflection Polarized Flux	N_G
7.652E-01	**2.165E-08**	1.051E-07	**5.62E+13**
7.513E-01	**6.180E-24**	1.975E-15	
7.513E-01	**9.103E-26**	2.398E-16	

Polarization by Reflection	Scattering Polarized Flux	Reflection Polarized Flux	N_D
7.652E-01	**2.165E-14**	1.051E-09	**3.16E+16**
7.513E-01	**6.180E-30**	1.975E-17	
7.513E-01	**9.103E-32**	2.398E-18	

Result

Wavelength	Total Polarized Flux	Total Flux	Total Polarization
4.00E-04	1.404E+06	5.103E+06	2.75E-01
3.60E-02	1.114E-03	1.530E-03	7.279E-01
6.10E-02	1.851E-05	6.225E-05	2.973E-01